AD-A050 060 AIR FORCE INST OF TECH WRIGHT-PATTERSON AFB OHIO F/G 4/2
A STUDY OF THE CHARACTERISTICS OF THE DATA SYSTEMS TEST KINEMAT--ETC(U)
AUG 77 A J MCGLASSON

UNCLASSIFIED AFIT-CI-78-32 NL

1 OF 1
AD A050 060

END
DATE FILMED
3-78
DDC

78-32

(1)

SC

A STUDY OF THE CHARACTERISTICS OF THE DATA SYSTEMS TEST KINEMATIC FIELDS

by

Allan Joseph McGlasson

A thesis submitted to the faculty of the
University of Utah in partial fulfillment of the requirements
for the degree of

Master of Science

Department of Meteorology

University of Utah

August 1977

UNCLASSIFIED

SECURITY CLASSIFICATION OF THIS PAGE (When Data Entered)

REPORT DOCUMENTATION PAGE

READ INSTRUCTIONS BEFORE COMPLETING FORM

(14) 1. REPORT NUMBER: AFIT-CI-78-32

2. GOVT ACCESSION NO.

3. RECIPIENT'S CATALOG NUMBER

(9) 5. TYPE OF REPORT & PERIOD COVERED: Master's Thesis

4. TITLE (and Subtitle): (6) A Study of the Characteristics of the Data Systems Test Kinematic Fields.

6. PERFORMING ORG. REPORT NUMBER

7. AUTHOR(s): (10) Allan Joseph/McGlasson
Captain Allan J. McGlasson

8. CONTRACT OR GRANT NUMBER(s)

9. PERFORMING ORGANIZATION NAME AND ADDRESS
AFIT/CI Student at the University of Utah
Salt Lake City UT

10. PROGRAM ELEMENT, PROJECT, TASK AREA & WORK UNIT NUMBERS

11. CONTROLLING OFFICE NAME AND ADDRESS
AFIT/CI
WPAFB OH 45433

(11) 12. REPORT DATE: Aug [redacted] 77

13. NUMBER OF PAGES: 69 Pages (12) 79p.

14. MONITORING AGENCY NAME & ADDRESS (if different from Controlling Office)

15. SECURITY CLASS. (of this report): Unclassified

15a. DECLASSIFICATION/DOWNGRADING SCHEDULE

16. DISTRIBUTION STATEMENT (of this Report)
Approved for Public Release; Distribution Unlimited

17. DISTRIBUTION STATEMENT (of the abstract entered in Block 20, if different from Report)

18. SUPPLEMENTARY NOTES
APPROVED FOR PUBLIC RELEASE AFR 190-17.
For JERRAL F. GUESS, Captain, USAF
Director of Information, AFIT
James E. Skarst MSgt USAF
Deputy Director of Information

19. KEY WORDS (Continue on reverse side if necessary and identify by block number)

20. ABSTRACT (Continue on reverse side if necessary and identify by block number)

Ø12 2ØØ

DD FORM 1 JAN 73 1473 EDITION OF 1 NOV 65 IS OBSOLETE

UNCLASSIFIED

SECURITY CLASSIFICATION OF THIS PAGE (When Data Entered)

THE UNIVERSITY OF UTAH GRADUATE SCHOOL

SUPERVISORY COMMITTEE APPROVAL

of a thesis submitted by

Allan Joseph McGlasson

I have read this thesis and have found it to be of satisfactory quality for a master's degree.

6/15/77
Date

Julia N. Paegle
Julia N. Paegle
Chairman, Supervisory Committee

I have read this thesis and have found it to be of satisfactory quality for a master's degree.

6/15/77
Date

Jan Paegle
Jan Paegle
Member, Supervisory Committee

I have read this thesis and have found it to be of satisfactory quality for a master's degree.

6/30/77
Date

Elford G. Astling
Elford G. Astling
Member, Supervisory Committee

THE UNIVERSITY OF UTAH GRADUATE SCHOOL

FINAL READING APPROVAL

To the Graduate Council of The University of Utah:

I have read the thesis of Allan Joseph McGlasson in its final form and have found that (1) its format, citations, and bibliographic style are consistent and acceptable; (2) its illustrative materials including figures, tables, and charts are in place; and (3) the final manuscript is satisfactory to the Supervisory Committee and is ready for submission to the Graduate School.

6/15/77
Date

Julia N. Paegle
Member, Supervisory Committee

Approved for the Major Department

S.K. Kao
Chairman/Dean

Approved for the Graduate Council

Sterling M. McMurrin
Dean of The Graduate School

ABSTRACT

Winter 1976 Data Systems Test wind data was used to produce a number of global kinematic fields. The data was prepared by the Goddard Institute for Space Studies Atmospheric General Circulation Model. An interpolation scheme was developed to move the wind data from sigma levels to constant pressure levels. Time-averaged fields of the zonal wind component, meridional wind component, divergence, vorticity, steady energy and transient energy were computed for 200 mb, 500 mb and 850 mb. In addition, the standing kinetic energy and transient kinetic energy were decomposed by wavenumbers into energy spectra for 200 mb and 500 mb for different latitudes.

Results of this research were compared with other similar studies and showed favorable correlation. Resolution of synoptic scale features was good. Organized areas were found in the time-averaged divergence fields indicating that divergence features can be resolved in this data. This study shows that the Goddard Model is well suited for global studies of the general atmospheric circulation.

ACKNOWLEDGEMENTS

I would like to express my sincere appreciation to Dr. Julia Paegle for all the help and time she gave me during the preparation of this thesis. In addition, I want to thank Drs. Jan Paegle and Elford Astling for their suggestions which helped improve this thesis and for their interest in this work.

I also want to thank my wife and children for all the love and patience they gave me during my work on this thesis. Special thanks are due my wife for typing the draft copy and to Michael for delaying his arrival until after I had finished my thesis defense.

A special thanks is also due Fred Lewis for his programing assistance and his preparation of the data into horizontal arrays. Finally, I want to express my appreciation to Dr. William Quirk and the Goddard Institute for Space Studies for supplying the data for this research and for providing valuable information about the data and its preparation.

TABLE OF CONTENTS

LIST OF FIGURES

Page

CHAPTER I

INTRODUCTION

The general circulation of the atmosphere is still not well understood. Lorenz (1967) mentions that even though there have been over a thousand excellent studies on the subject, a full explanation of the distribution of the atmospheric wind patterns is lacking. The atmosphere is so vast and motions in it are so complex that it was impossible to collect global circulation data until this century. It is obvious from our current knowledge of the atmosphere that to successfully unravel this mystery we need more clues.

The clues in this case are more complete data sets. Data is needed for the entire globe at several levels in the atmosphere. The only way that the required volumes of data can be collected is through international cooperation of countries. Although much data is collected and exchanged daily by many countries, it is not sufficient for the task of fully explaining the general circulation.

Meteorologists recognized several years ago that it was time to formulate a plan for gathering more detailed global data. As a result, the Global Atmospheric Research Project (GARP) was formulated. GARP will be the most intensive effort yet to collect and analyze atmospheric data for the entire globe. It will involve many countries, thousands of scientists and much sophisticated equipment when it is implemented at the end of this decade.

To be useful, the massive amount of data which will be generated by GARP will have to be placed into a format which will allow computer analysis. The Goddard Institute for Space Studies (GISS) Nine-Level Atmospheric General Circulation Model has been selected for this data preparation. This study uses a set of data generated by the GISS model.

The objective of this study was to compare the data prepared by the GISS model to data from other sources. This was done partly to assess the quality of the data produced by the model and partly to get a feel for what type features can be resolved by this data. The analysis of the data was divided into two basic areas. First, a number of time-averaged fields were generated. These included time-averaged wind components, divergences and vorticities. The second area of study involved a wave number decomposition of the kinetic energy for the standing and transient eddies. The period covered by the data (one month) was too short to consider any attempt to add to the theory of the general circulation. However, this study gives an indication of the type and amount of data which will soon be available.

CHAPTER II

DESCRIPTION AND TREATMENT OF DATA

Global, synoptic scale wind data, which covers 35 days at 12 hour intervals, was used for this analysis. The data covers the period from 00Z/29 JAN 76 until 12Z/3 MAR 76. It was prepared by the GISS atmospheric circulation model and is designated Data System Test (DST) data. The model uses five primary quantities to represent the behaviour of the atmosphere: u--the zonal wind speed (west to east), v--the meridional wind speed (south to north), T--the temperature, q--the specific humidity of water vapor, and π--the surface pressure minus the pressure at the top of the model. This study used only the u, v, and π data. Three forcing terms are included in the differential equations used by the model to update the primary quantities. These terms are designed to represent the physical processes of earth-atmosphere and sun-atmosphere interaction and include a horizontal frictional force term, a diabatic heating rate term, and a rate of moisture addition term. For detailed information on the GISS model consult Somerville et al. (1974).

The model uses a split global grid in spherical coordinates. The grid is diagramed in Figure 1. The primary grid points, denoted by o's, contain T, q, and π data while u and v data is carried at the secondary grid points, the +'s. The poles are primary grid points, while the equator is at secondary grid points. Grid points are spaced every four degrees of latitude and every five degrees of longitude on

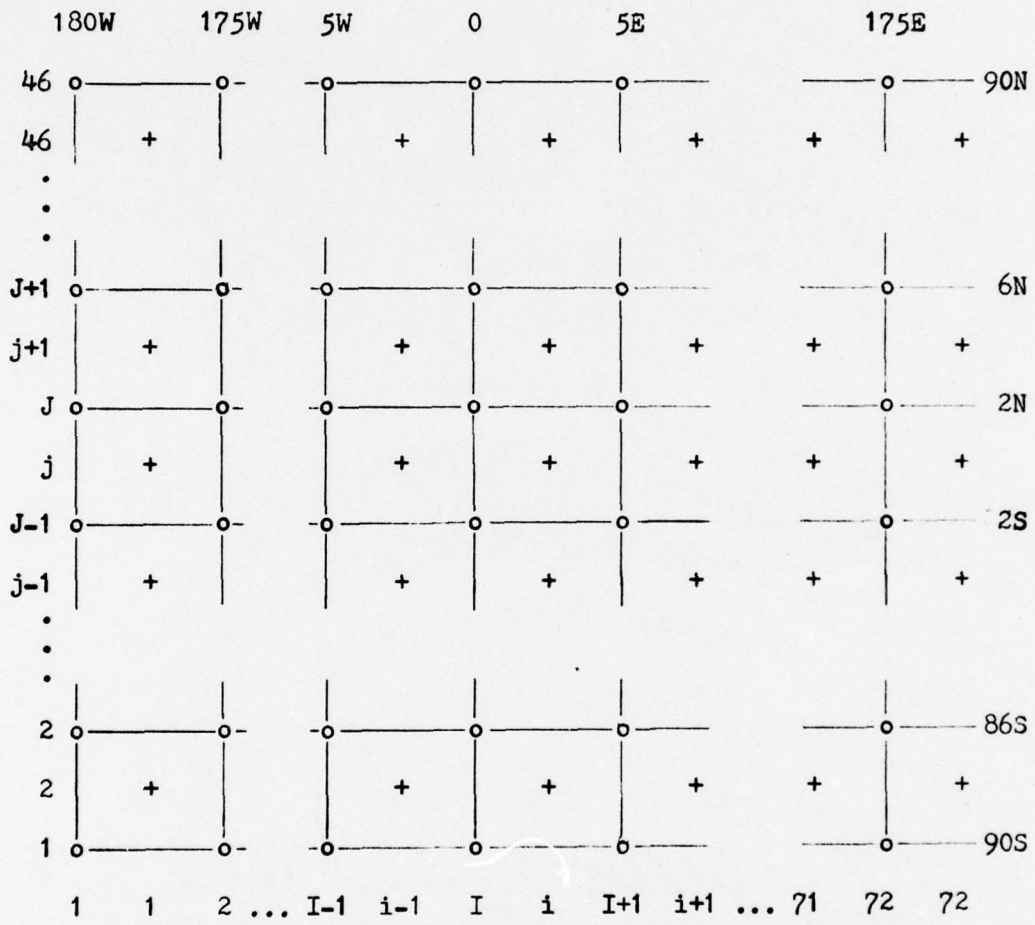

Figure 1 GISS Model Grid. Primary grid points are represented by o's while the +'s denote secondary grid points.

both grids. This makes a total of 3312 points over the globe per grid. The primary grid has 46 points from pole to pole and 72 points around a latitude circle.

The secondary grid contains the same number of points, but the row which falls below the South Pole is meaningless so it only has 45 meaningful latitude circles. Figures 2 and 3 show the primary grid for the Northern Hemisphere and Southern Hemisphere respectively with the topography used by the model given in meters.

A sigma vertical coordinate system is used. Sigma (σ) is defined by

$$\sigma = \frac{P-P_T}{P_S-P_T} = \frac{P-P_T}{\pi} \qquad (2.1)$$

where P is the pressure at the level of measurement,

P_S is the surface pressure at the grid point,

P_T is the pressure at the top of the atmosphere.

Note: P_T is 10 mb in this model. There are nine levels above the surface with sigma at each level (σ_ℓ) given by Equation (2.2).

$$\sigma_\ell = \frac{\ell-.5}{9}, \quad \ell = 1, 2\cdots 9. \qquad (2.2)$$

Level one is the highest level and nine is the lowest. Note that σ is zero at the top of the atmosphere and one at the surface.

Sigma Coordinates Over Mountains

Divergence fields at constant pressure were computed at several sigma levels using the following equation for divergence:

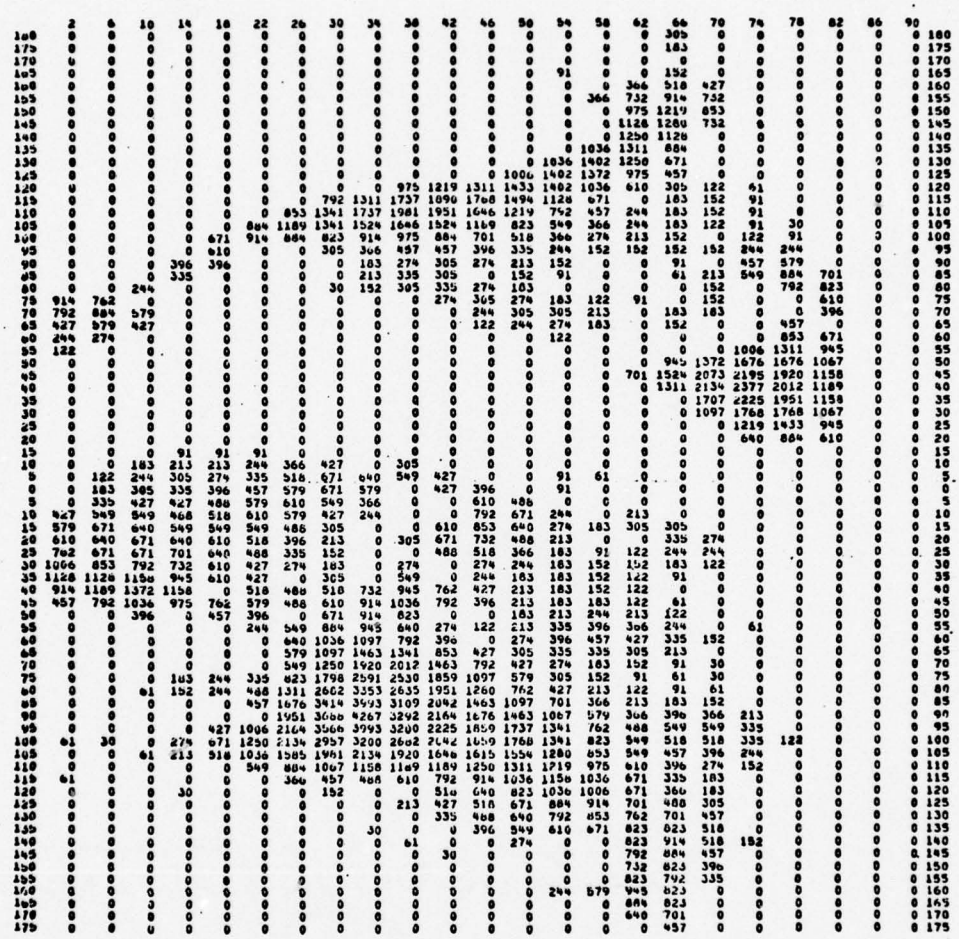

Figure 2 GISS Model Northern Hemisphere Topography Terrain heights are given in meters.

	-90	-86	-82	-78	-74	-70	-66	-62	-58	-54	-50	-46	-42	-38	-34	-30	-26	-22	-18	-14	-10	-6	-2	
180	2469	1524	0	0	0	0	0	0	0	0	0	0	0	0	0	0	0	0	0	0	0	0	0	180
175	2469	1494	0	0	0	0	0	0	0	0	0	0	0	0	0	0	0	0	0	0	0	0	0	175
170	2469	1463	0	0	0	0	0	0	0	0	0	0	0	0	0	0	0	0	0	0	0	0	0	170
165	2469	1433	0	0	0	0	0	0	0	0	0	0	0	0	0	0	0	0	0	0	0	0	0	165
160	2469	1402	0	0	0	0	0	0	0	0	0	0	0	0	0	0	0	0	0	0	0	0	0	160
155	2469	1433	0	61	0	0	0	0	0	0	0	0	0	0	0	0	0	0	0	0	0	0	0	155
150	2469	1494	610	183	0	0	0	0	0	0	0	0	0	0	0	0	0	0	0	0	0	0	0	150
145	2469	1554	762	305	0	0	0	0	0	0	0	0	0	0	0	0	0	0	0	0	0	0	0	145
140	2469	1554	884	457	0	0	0	0	0	0	0	0	0	0	0	0	0	0	0	0	0	0	0	140
135	2469	1615	1036	640	0	0	0	0	0	0	0	0	0	0	0	0	0	0	0	0	0	0	0	135
130	2469	1676	1189	853	0	0	0	0	0	0	0	0	0	0	0	0	0	0	0	0	0	0	0	130
125	2469	1768	1311	1066	518	0	0	0	0	0	0	0	0	0	0	0	0	0	0	0	0	0	0	125
120	2469	1920	1402	975	488	0	0	0	0	0	0	0	0	0	0	0	0	0	0	0	0	0	0	120
115	2469	2073	1524	884	0	0	0	0	0	0	0	0	0	0	0	0	0	0	0	0	0	0	0	115
110	2469	2256	1676	914	0	0	0	0	0	0	0	0	0	0	0	0	0	0	0	0	0	0	0	110
105	2469	2377	1859	1067	0	0	0	0	0	0	0	0	0	0	0	0	0	0	0	0	0	0	0	105
100	2469	2438	1951	1219	488	0	0	0	0	0	0	0	0	0	0	0	0	0	0	0	0	0	0	100
95	2469	2377	1920	1280	610	0	0	0	0	0	0	0	0	0	0	0	0	0	0	0	0	0	0	95
90	2469	2225	1737	1189	610	0	0	0	0	0	0	0	0	0	0	0	0	0	0	0	0	0	0	90
85	2469	1981	1402	914	488	0	0	0	0	0	0	0	0	0	0	0	0	0	0	0	0	0	0	85
80	2469	1798	1097	671	366	0	0	0	0	0	0	0	0	0	0	0	0	0	0	0	0	884	823	80
75	2469	1707	914	579	488	0	0	0	0	0	427	610	518	0	0	0	0	0	0	1585	1524	1158	945	75
70	2469	1676	884	640	792	671	0	0	0	183	427	549	610	671	945	1311	1554	1707	1951	2042	1463	762	579	70
65	2469	1707	853	549	732	701	366	0	0	0	0	0	305	518	823	1128	1372	1494	1524	1280	762	335	244	65
60	2469	1737	792	0	0	0	0	0	0	0	0	0	0	152	274	396	518	610	640	549	335	183	183	60
55	2469	1737	762	0	0	0	0	0	0	0	0	0	0	0	61	122	244	335	396	366	274	213	152	55
50	2469	1768	762	0	0	0	0	0	0	0	0	0	0	0	0	0	213	396	457	427	335	213	122	50
45	2469	1798	823	0	0	0	0	0	0	0	0	0	0	0	0	0	0	335	488	457	366	213	91	45
40	2469	1859	914	0	0	0	0	0	0	0	0	0	0	0	0	0	0	0	274	335	274	183	0	40
35	2469	1981	1097	0	0	0	0	0	0	0	0	0	0	0	0	0	0	0	0	0	91	0	0	35
30	2469	2103	1372	610	0	0	0	0	0	0	0	0	0	0	0	0	0	0	0	0	0	0	0	30
25	2469	2225	1676	1006	0	0	0	0	0	0	0	0	0	0	0	0	0	0	0	0	0	0	0	25
20	2469	2347	1981	1494	823	0	0	0	0	0	0	0	0	0	0	0	0	0	0	0	0	0	0	20
15	2469	2469	2286	1890	1158	0	0	0	0	0	0	0	0	0	0	0	0	0	0	0	0	0	0	15
10	2469	2560	2438	2164	1341	0	0	0	0	0	0	0	0	0	0	0	0	0	0	0	0	0	0	10
5	2469	2652	2621	2408	1615	0	0	0	0	0	0	0	0	0	0	0	0	0	0	0	0	0	0	5
0	2469	2713	2743	2621	1951	914	0	0	0	0	0	0	0	0	0	0	0	0	0	0	0	0	0	0
-5	2469	2774	2865	2804	2225	1158	0	0	0	0	0	0	0	0	0	0	0	0	0	0	0	0	0	-5
-10	2469	2804	2957	2926	2347	1219	0	0	0	0	0	0	0	0	0	0	0	0	0	0	0	0	305	-10
-15	2469	2865	3048	3016	2408	1280	0	0	0	0	0	0	0	0	0	0	518	701	792	823	732	610	549	-15
-20	2469	2926	3139	3078	2438	1280	0	0	0	0	0	0	0	0	213	518	823	975	1067	1097	1036	853	671	-20
-25	2469	2987	3231	3139	2499	1311	0	0	0	0	0	0	0	0	0	671	914	914	945	1006	1036	1006	884	-25
-30	2469	3018	3292	3200	2560	1341	0	0	0	0	0	0	0	0	0	518	671	671	732	853	975	1128	1128	-30
-35	2469	3048	3322	3292	2652	1433	0	0	0	0	0	0	0	0	0	0	0	335	427	549	701	945	1097	-35
-40	2469	3078	3353	3322	2743	1554	0	0	0	0	0	0	0	0	0	0	0	0	0	0	0	488	671	-40
-45	2469	3109	3383	3322	2804	1707	0	0	0	0	0	0	0	0	0	0	0	0	152	183	0	0	0	-45
-50	2469	3109	3353	3231	2743	1859	792	0	0	0	0	0	0	0	0	0	0	0	0	0	122	0	0	-50
-55	2469	3109	3292	3109	2591	1768	792	0	0	0	0	0	0	0	0	0	0	0	0	0	0	0	0	-55
-60	2469	3139	3261	2926	2286	1402	0	0	0	0	0	0	0	0	0	0	0	0	0	0	0	0	0	-60
-65	2469	3139	3261	2835	2012	1067	0	0	0	0	0	0	0	0	0	0	0	0	0	0	0	0	0	-65
-70	2469	3170	3322	2865	1981	0	0	0	0	0	0	0	0	0	0	0	0	0	0	0	0	0	0	-70
-75	2469	3170	3383	3048	2225	1128	0	0	0	0	0	0	0	0	0	0	0	0	0	0	0	0	0	-75
-80	2469	3170	3414	3231	2591	1463	0	0	0	0	0	0	0	0	0	0	0	0	0	0	0	0	0	-80
-85	2469	3170	3444	3383	2896	1737	0	0	0	0	0	0	0	0	0	0	0	0	0	0	0	0	0	-85
-90	2469	3139	3444	3444	3048	1951	0	0	0	0	0	0	0	0	0	0	0	0	0	0	0	0	0	-90
-95	2469	3109	3414	3444	3078	2103	884	0	0	0	0	0	0	0	0	0	0	0	0	0	0	0	0	-95
-100	2469	3078	3383	3383	3018	2134	975	0	0	0	0	0	0	0	0	0	0	0	0	0	0	0	0	-100
-105	2469	3018	3261	3292	2926	2012	853	0	0	0	0	0	0	0	0	0	0	0	0	0	0	0	61	-105
-110	2469	2957	3170	3170	2835	1829	0	0	0	0	0	0	0	0	0	0	0	0	0	0	0	0	0	-110
-115	2469	2926	3078	3109	2804	1768	0	0	0	0	0	0	0	0	0	0	122	91	0	0	0	0	61	-115
-120	2469	2896	3018	3018	2774	1768	0	0	0	0	0	0	0	0	30	152	244	213	0	0	0	0	0	-120
-125	2469	2835	2926	2957	2713	1829	0	0	0	0	0	0	0	0	0	213	305	274	152	0	0	0	0	-125
-130	2469	2774	2835	2835	2682	1920	853	0	0	0	0	0	0	0	0	213	305	305	183	61	0	0	0	-130
-135	2469	2743	2713	2713	2560	1859	823	0	0	0	0	0	0	0	0	213	274	274	183	61	0	0	0	-135
-140	2469	2682	2621	2560	2377	1615	0	0	0	0	0	0	0	0	152	244	244	213	152	0	0	366	0	-140
-145	2469	2591	2499	2408	2164	1372	0	0	0	0	0	0	30	0	213	305	244	183	91	0	0	366	0	-145
-150	2469	2530	2377	2256	1981	1189	0	0	0	0	0	0	0	0	183	244	183	0	0	0	122	0	0	-150
-155	2469	2408	2164	2012	1707	975	0	0	0	0	0	0	0	0	0	0	0	0	0	0	0	0	0	-155
-160	2469	2103	1554	1341	1189	671	0	0	0	0	0	0	0	0	0	0	0	0	0	0	0	0	0	-160
-165	2469	1737	0	0	488	0	0	0	0	0	0	0	0	0	0	0	0	0	0	0	0	0	0	-165
-170	2469	1585	0	0	0	0	0	0	0	0	0	0	61	0	0	0	0	0	0	0	0	0	0	-170
-175	2469	1524	0	0	0	0	0	0	0	0	0	0	0	30	0	0	0	0	0	0	0	0	0	-175

Figure 3 GISS Model Southern Hemisphere Topography Terrain heights are given in meters.

$$\nabla_p \cdot \mathbf{V} = \frac{1}{a}\left[\frac{1}{\cos\phi}\frac{\partial u}{\partial \lambda} + \frac{\partial v}{\partial \phi} - v\tan\phi\right]$$

$$-\frac{\sigma}{\pi}\left[\frac{\partial u}{\partial \sigma}\left(\frac{1}{a\cos\phi}\frac{\partial \pi}{\partial \lambda}\right) + \frac{\partial v}{\partial \sigma}\left(\frac{1}{a}\frac{\partial \pi}{\partial \phi}\right)\right]. \qquad (2.3)$$

The finite difference form of Equation (2.3) which was used is

$$(\nabla_p \cdot \mathbf{V})_{i,j} = \frac{1}{a}\left[\frac{1}{\cos\phi_j}\frac{u_{i+1,j} - u_{i-1,j}}{\Delta\lambda} + \frac{v_{i,j+1} - v_{i,j-1}}{\Delta\phi}\right.$$

$$\left. - v_{i,j}\tan\phi\right] - \frac{\sigma}{\pi}\left[\frac{u^{\ell+1}_{i,j} - u^{\ell-1}_{i,j}}{\Delta\sigma}\left(\frac{1}{a\cos\phi_j}\frac{\pi_{i+1,j} - \pi_{i-1,j}}{\Delta\lambda}\right)\right.$$

$$\left. + \frac{v^{\ell+1}_{i,j} - v^{\ell-1}_{i,j}}{\Delta\sigma}\left(\frac{1}{a}\frac{(\pi_{i,j+1} - \pi_{i,j-1})}{\Delta\phi}\right)\right]. \qquad (2.4)$$

After examining these fields, it was suspected that the values over the mountains were spurious. Thus, the following test was conducted. A vertical wind profile, constant at a given pressure, was selected and entered at all grid points. Figure 4 illustrates the wind profile. The divergence was then computed for several sigma levels for the π field of 00Z/8 FEB 76 using Equation (2.4). Values over the oceans were small (order 10^{-8} sec^{-1} or smaller) as they should have been. However, over mountains such as the Andes, values on the order of 10^{-6} sec^{-1} were obtained. These values occurred because of the steep slopes of the sigma surfaces as they cross over the mountains. It is not possible to correctly approximate the derivatives involved by finite differences for the coarse grid used in this version of the GISS model. At this point the decision was made to interpolate the wind data to constant pressure levels to partially circumvent this problem.

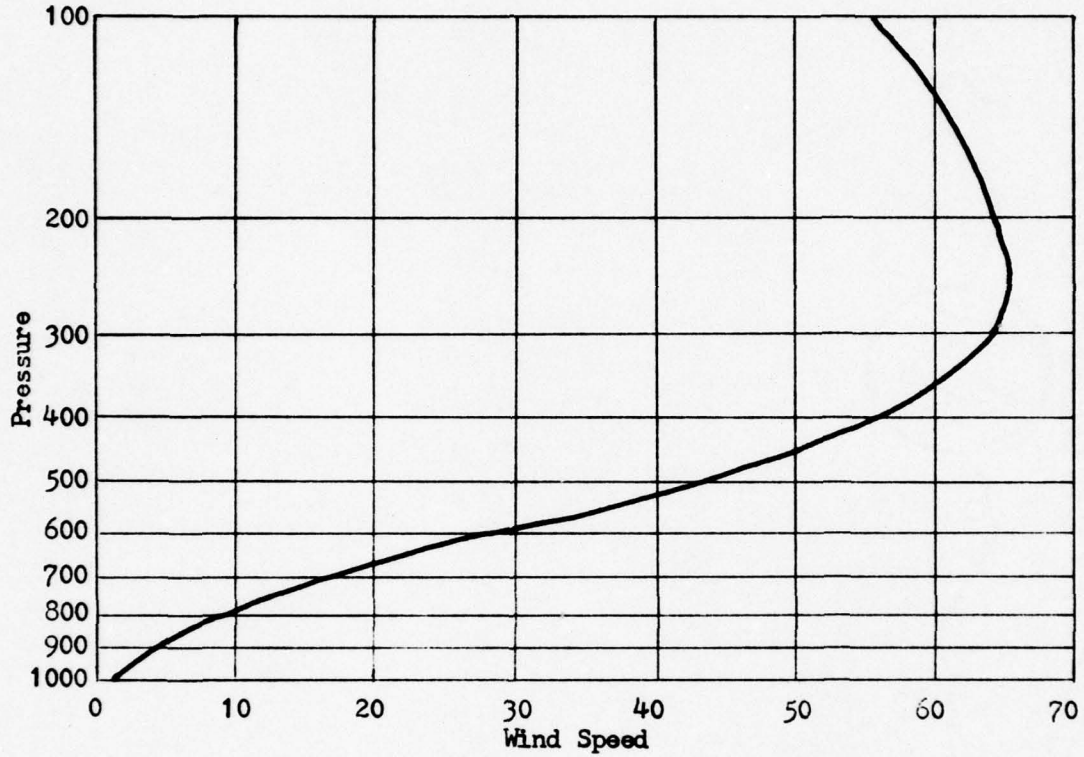

Figure 4 Test Wind Profile--wind speed is in m/sec, pressure is in mb.

Interpolation Scheme

Although the advantages of sigma coordinates are well known, (Phillips,1957), having the data on constant sigma surfaces proved to be inconvenient for this study. As seen in the previous section, it was not possible to produce meaningful divergence fields on constant sigma surfaces in the vicinity of mountains. Also, if the data was analyzed at constant sigma levels, it could not be readily compared with other data since most analyses of the type performed here are done at constant pressure levels. For these reasons the decision was made to interpolate the data from the sigma levels to constant pressure levels. Three levels were chosen for study, 200 mb, 500 mb, and 850 mb.

A cubic spline was used for the interpolation from sigma levels to constant pressure levels. The spline was essentially the one contained in Conte and de Boor (1965). The procedure involves constructing a piecewise-cubic polynomial which interpolates the function at each of the known points. This is done by constructing a certain cubic polynomial of the form

$$P_i(x) = a_{1,i} + a_{2,i}x + a_{3,i}x^2 + a_{4,i}x^3 \qquad (2.5)$$

for each sub-interval so that the resulting piece-wise cubic interpolant is twice continuously differentiable,

$$P''_{i-1}(x_i) = P''_i(x_i) \ , \ i=2, 3, \cdots N-1$$

where N is the number of known points. A piece-wise cubic interpolant of this form is known as a cubic spline.

The subroutine developed for use in this interpolation required

knowledge of the function values at each known point plus the slope of the function at the two end points. The end point slopes were found by finding the derivative of a quadratic polynomial passing through the end point and the two adjacent points. The subroutine then used Gauss elimination to solve for the coeffecients $a_{1,i}$, $a_{2,i}$, $a_{3,i}$ and $a_{4,i}$ of Equation (2.5). A minimum of four points are needed for the cubic spline of this subroutine.

To interpolate the winds to constant pressure levels it was necessary to have π values at the secondary grid points. These values were derived by summing the π values at the four primary points surrounding a secondary point and dividing by four. Though simple, this procedure produced acceptable results.

Once the π value at a secondary grid point was known, the pressure at each sigma level was computed. The nine pressure values were then passed to the spline as the x_i values and the wind components at each level were passed as the $f(x_i)$ values. The cubic spline then computed $f(x)$ values at 200 mb, 500 mb, and 850 mb.

For levels which were below ground, a value of 999999 was assigned as a flag. The effect of this flagging appears in the 850 mb charts presented in the following chapter.

The cubic spline was tested on several known functions. Table 1 shows the functions, the exact value of the function, and the interpolated value of the function, and the error. From the results one can see that the cubic spline is sufficiently accurate for any reasonably smooth wind profile. The results presented in the next chapters suggest that this interpolation scheme was very successful.

TABLE 1

Test Results for Cubic Spline

Pressure Level (mb)	Exact Value (m/sec)	Interpolated Value (m/sec)	Error (m/sec)	Exact Value (m/sec)	Interpolated Value (m/sec)	Error (m/sec)
	Function=10 ln((1050-P)/100)			Function=50 cos(P/100)		
100	22.51	22.51	.208-02	23.43	27.02	.359+01
200	21.40	21.40	.547-03	-19.75	-20.81	.106+01
300	20.15	20.15	.298-03	-49.59	-49.50	.875-01
400	18.72	18.72	.240-03	-32.66	-32.68	.260-01
500	17.05	17.05	.162-03	14.17	14.18	.149-01
600	15.04	15.04	.169-02	47.98	48.01	.295-01
700	12.52	12.53	.122-01	37.73	37.70	.327-01
800	9.22	9.16	.573-01	-7.99	-7.28	.711+00
900	3.82	4.05	.238+00	-42.74	-45.56	.282+01
	Function=$((1500-P)/500)^4$			Function=sinh((1400-P)/275)		
100	61.51	61.47	.399-01	56.67	56.49	.179+00
200	45.69	45.70	.105-01	39.22	39.26	.491-01
300	33.18	33.18	.234-02	27.30	27.29	.103-01
400	23.43	23.43	.472-03	18.96	18.96	.206-02
500	16.00	16.00	.355-04	13.17	13.17	.130-03
600	10.50	10.50	.157-03	9.14	9.14	.142-03
700	6.55	6.55	.106-02	6.33	6.34	.980-03
800	3.85	3.84	.461-02	4.38	4.37	.321-02
900	2.05	2.07	.190-01	2.99	3.00	.138-01

CHAPTER III

TIME-AVERAGED FIELDS

Time-averaged fields of several quantities were constructed for 200 mb, 500 mb, and 850 mb levels. These fields are presented in this chapter with a discussion of how they compare with similar fields computed from other data. It should be noted that for both hemispheres positive values of u denote flows from west to east and positive v values indicate flows from south to north.

Wind Fields

For each grid point the time-averaged zonal and meridional wind components were defined in the usual manner with Equations (3.1) and (3.2).

$$\bar{u} = \frac{1}{T} \int_0^T u\,dt \tag{3.1}$$

$$\bar{v} = \frac{1}{T} \int_0^T v\,dt \tag{3.2}$$

u = zonal wind

$\bar{u}$ = time-averaged zonal wind

v = meridional wind

$\bar{v}$ = time-averaged meridional wind

T = time interval

The quantities $\bar{u}$ and $\bar{v}$ were evaluated by Equation (3.3);

$$\bar{x} = \frac{1}{N} \sum_{i=1}^{N} x_i \tag{3.3}$$

with x = u or v. For this sample N = 70. Figures 5, 6, and 7 show the $\bar{u}$ fields for 200 mb, 500 mb, and 850 mb respectively. Figures 8, 9, and 10 display the corresponding $\bar{v}$ fields. The asterisks on the 850 mb charts represent grid points where the 850 mb surface is below the surface of the earth in the model.

At each grid point the standard deviation (SD) for the above fields was also computed as follows:

$$SD = \{\frac{1}{N} [\sum_{i=1}^{N} x_i^2 - \frac{1}{N} (\sum_{i=1}^{N} x_i)^2]\}^{1/2} \tag{3.4}$$

where N = 70 and $x_i = u_i$ or v_i.

Figures 11 and 12 present the standard deviations of the $\bar{u}$ and $\bar{v}$ fields respectively at 500 mb. The standard deviations at the other levels showed similar patterns so they are not included.

A comparison of the time-averaged fields with fields from other data sets, (Van Loon, 1971), (Sadler, 1975), showed good agreement and indicated that the time-averaged wind patterns for February 1976 conformed closely to expected values. Some points of interest on the $\bar{u}$ charts, include the band of pronounced westerly flow at all levels in the Southern Hemisphere centered around 48° S latitude, the strong westerly flow at 200 mb in the Pacific centered about 4° S, and the easterly flow at 200 mb in the Southern Hemisphere tropics which seems

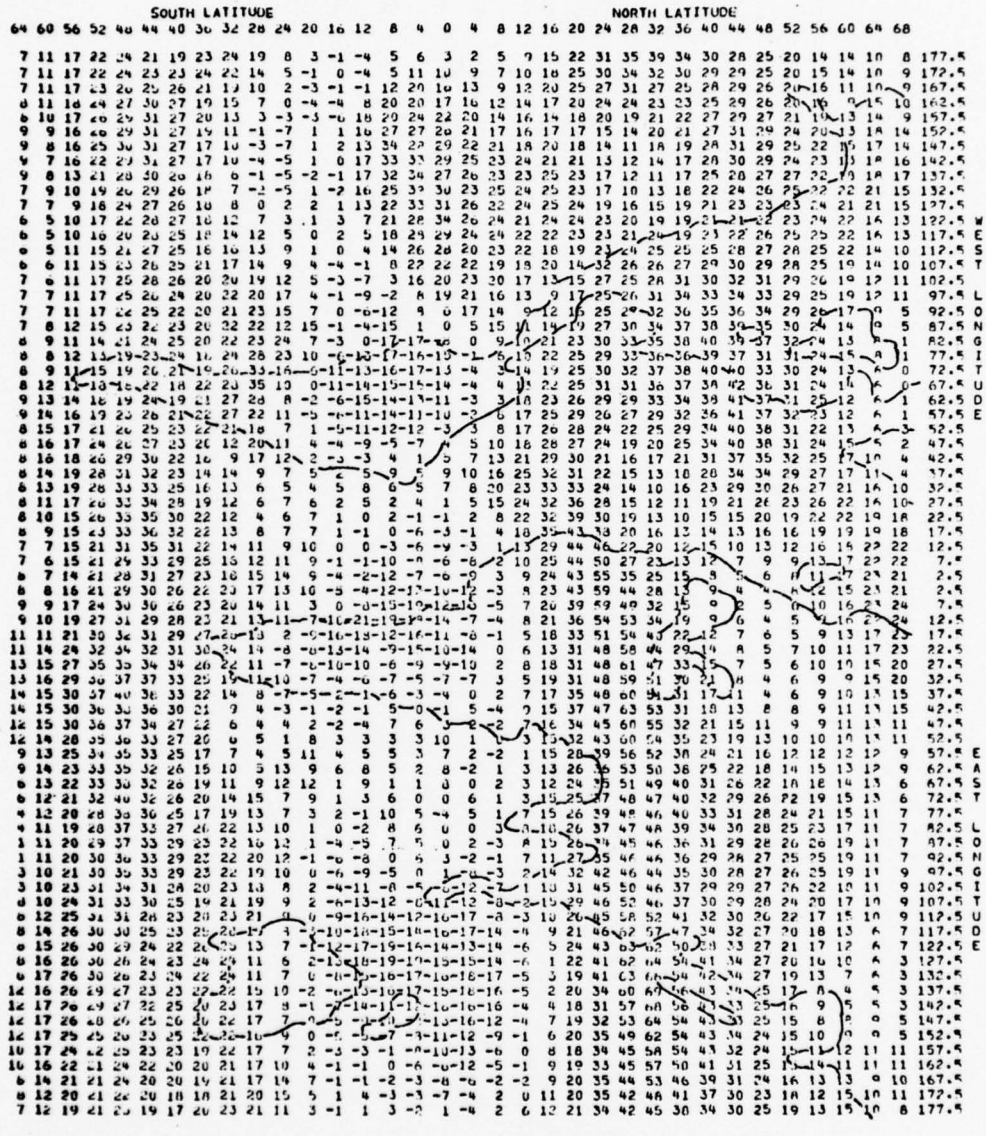

Figure 5 Time-average of u wind component at 200 mb (m/sec).

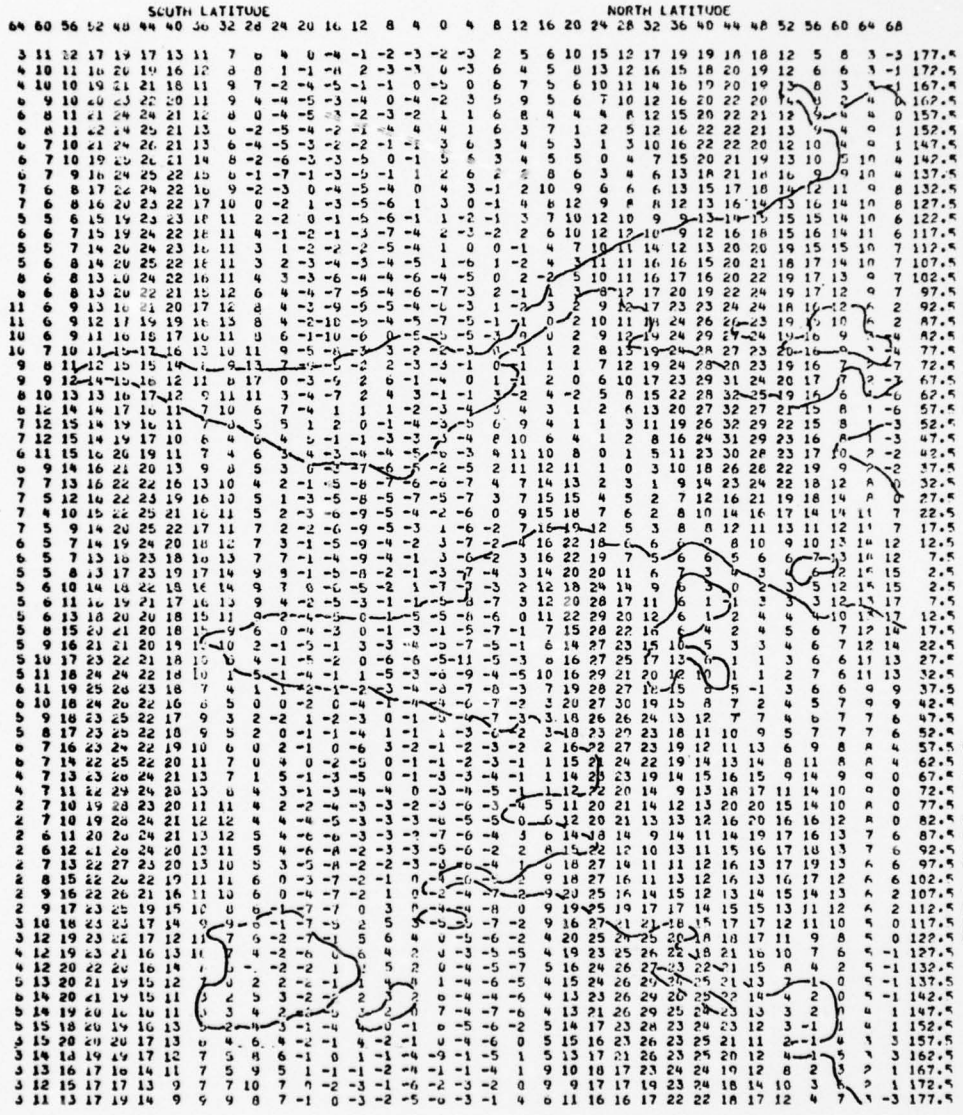

Figure 6 Time-average of u wind component at 500 mb (m/sec).

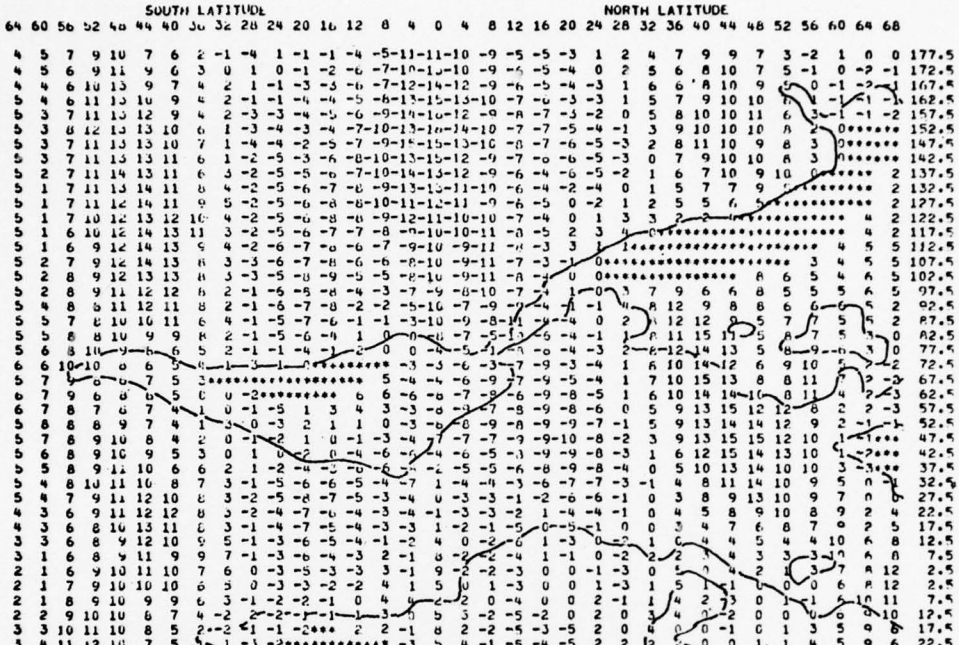

Figure 7 Time-average of u wind component at 850 mb (m/sec); asterisks indicate areas where 850 mb surface is below ground.

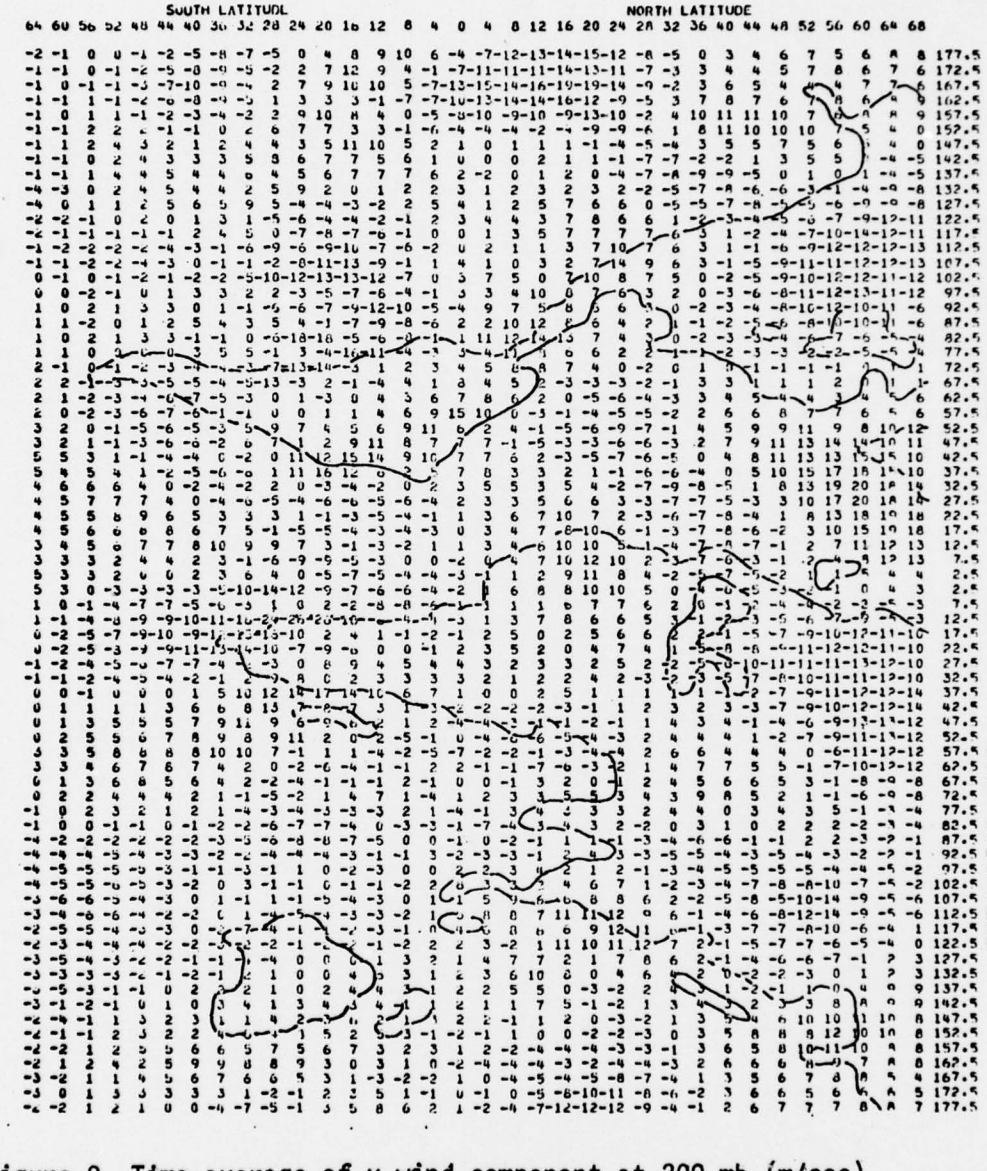

Figure 8 Time-average of v wind component at 200 mb (m/sec).

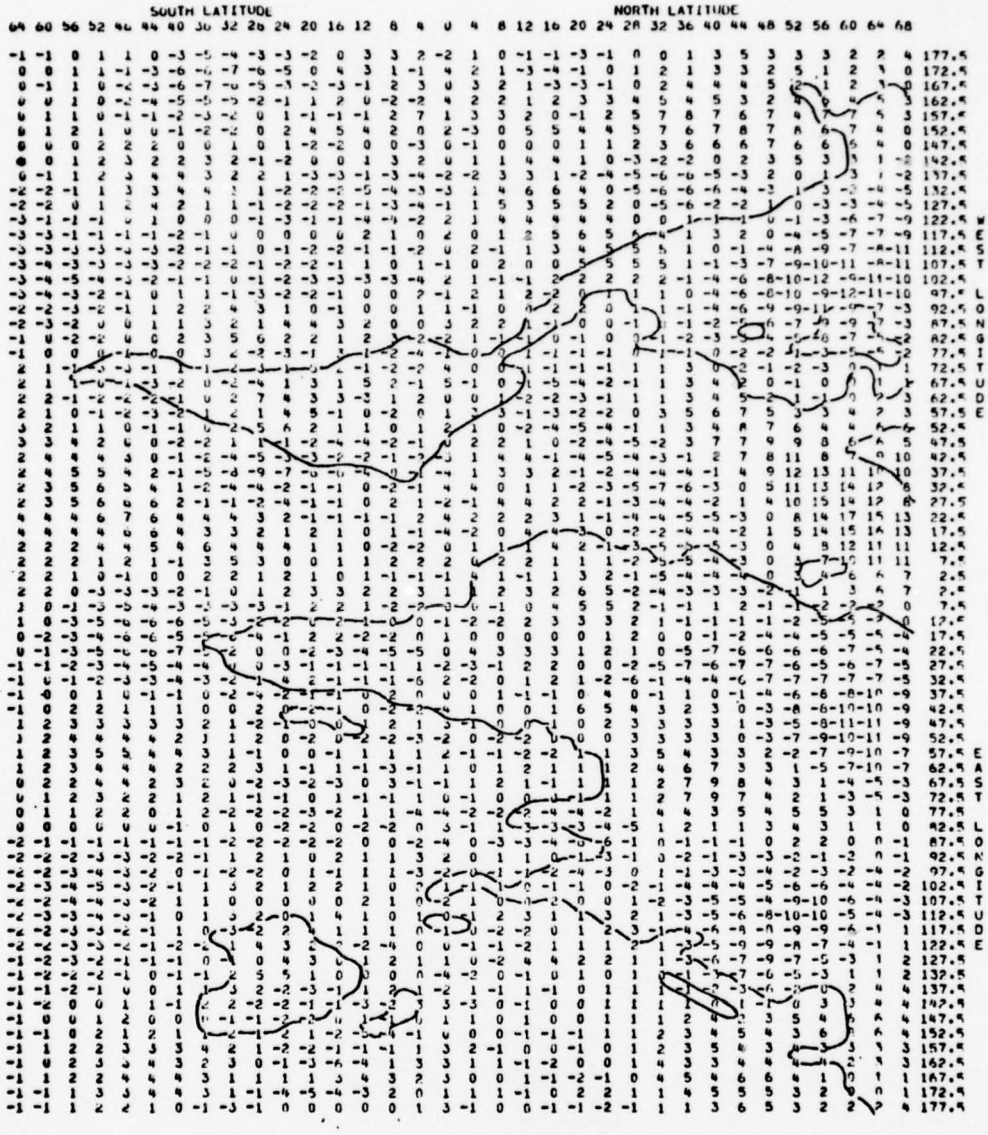

Figure 9 Time-average of v wind component at 500 mb (m/sec).

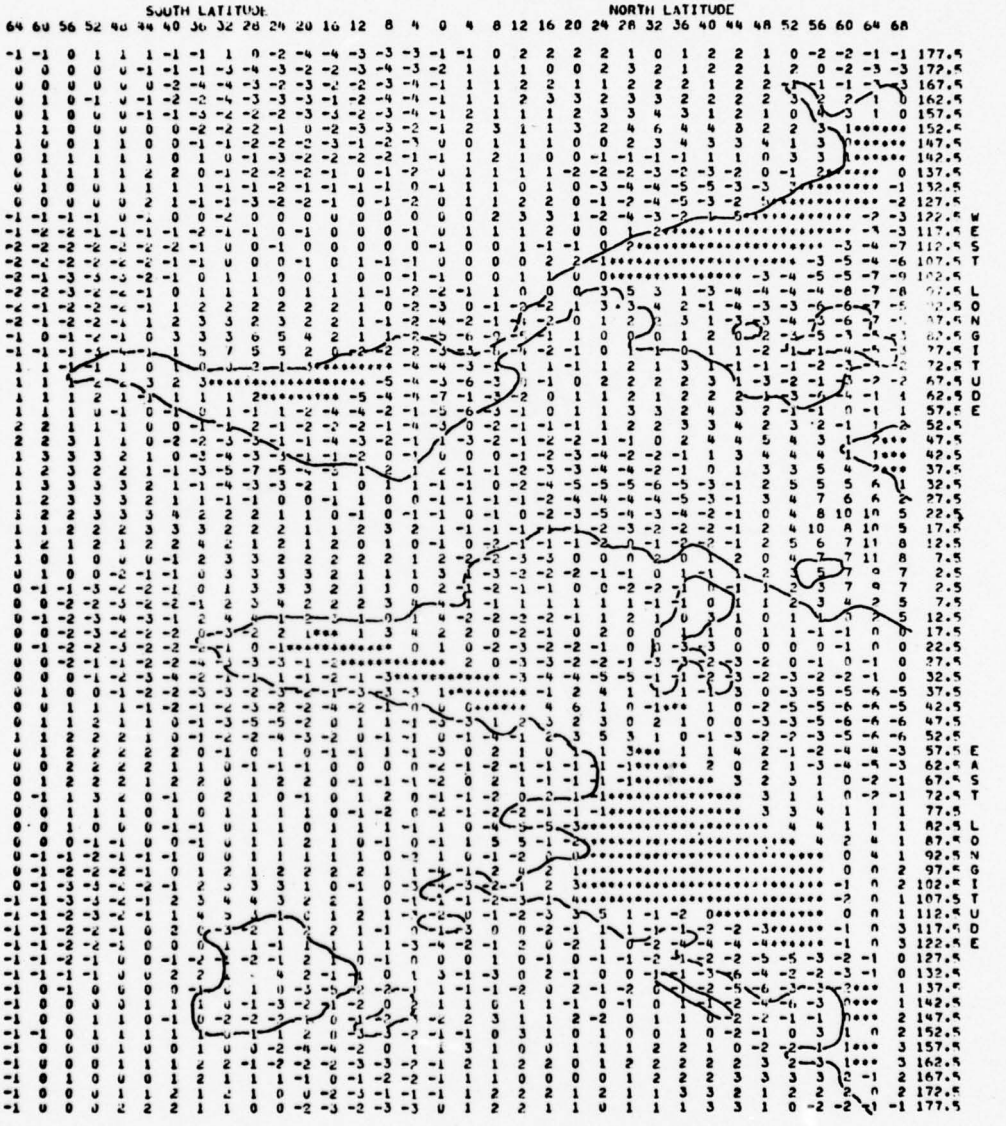

Figure 10 Time-average of v wind component at 850 mb (m/sec); asterisks indicate areas where 850 mb surface is below ground.

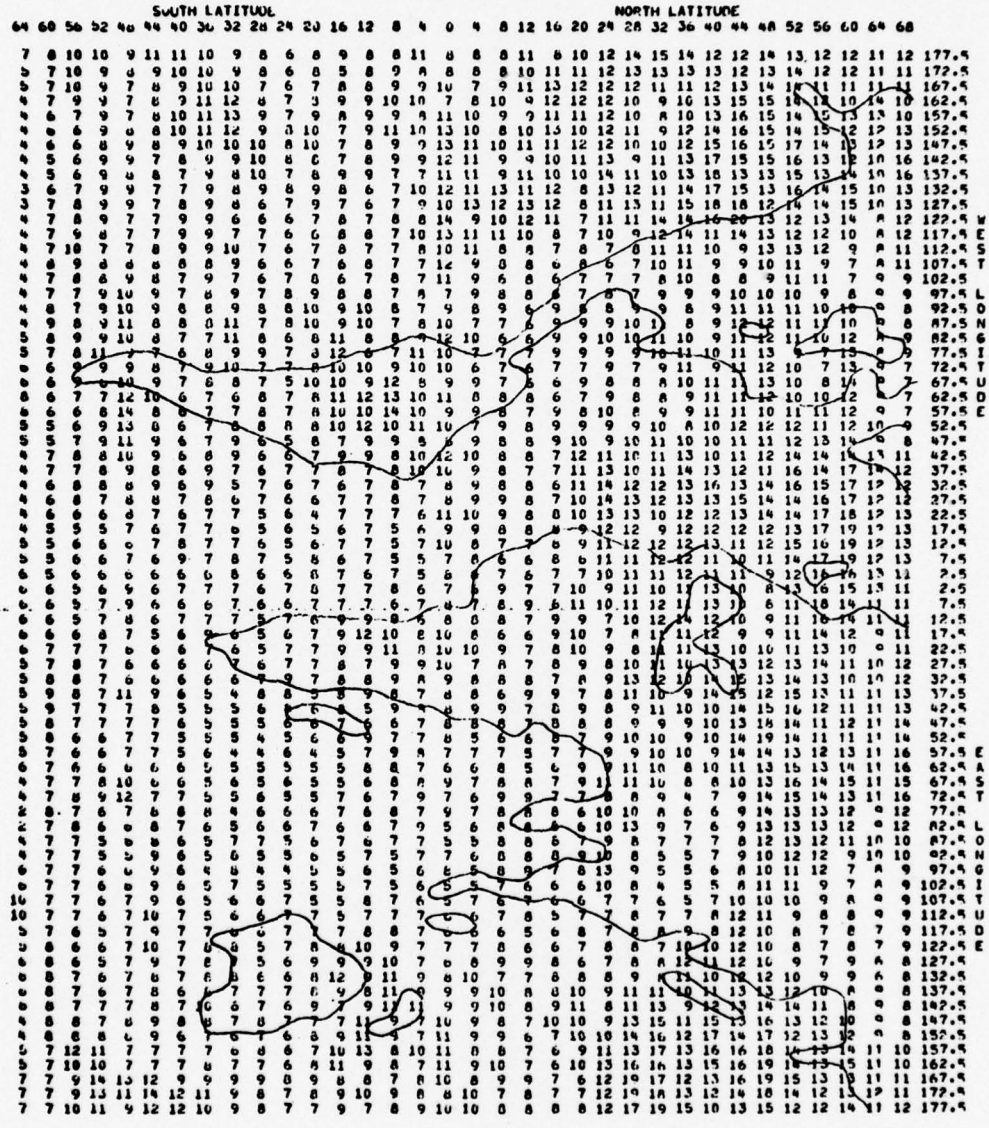

Figure 11 Standard deviation of time-averaged u wind component at 500 mb (m/sec).

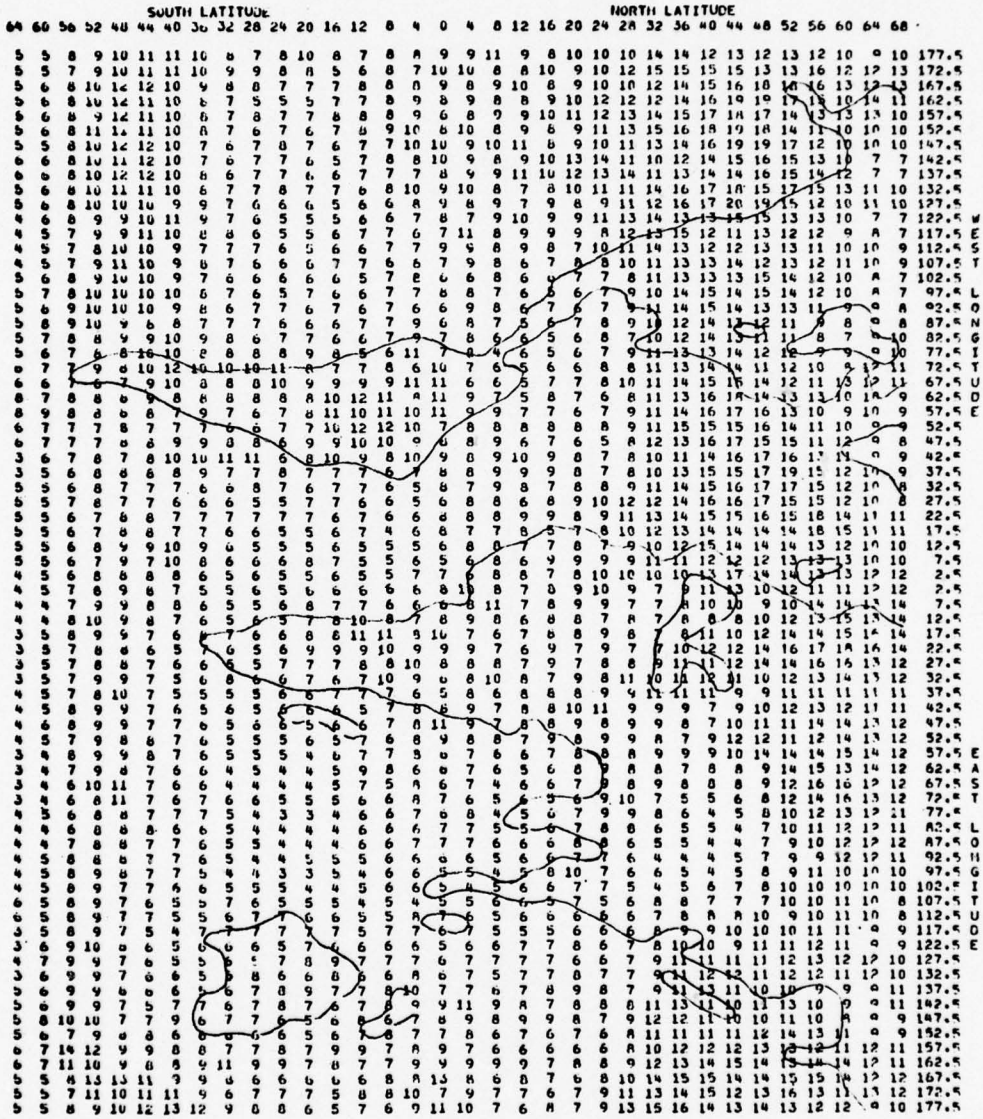

Figure 12 Standard deviation of time-averaged v wind component at 500 mb (m/sec).

to correspond with the continents. Also, the $\bar{u}$ fields show that the expected maximums of westerly flow in the Northern Hemisphere are visible at all levels. They occur along the eastern United States, over northern Africa, and off the coast of Asia.

Extensive easterly flow is evident at 850 mb throughout much of the tropics. This 850 mb easterly flow shows a distinct maximum near the equator under the maximum of the 200 mb westerly jet. This may represent the Walker circulation described by Krishnamurti et al. (1973).

At all levels standard deviations of $\bar{u}$ are generally smaller than the corresponding value of $\bar{u}$. For the 200 mb and 500 mb levels the SD values are 25 - 50 % of $\bar{u}$. The standard deviations of $\bar{v}$ are generally larger than $\bar{v}$ at all levels. Many SD values are twice the value of $\bar{v}$ and sometimes the SD is an order of magnitude larger than $\bar{v}$. The fact that $\bar{v}$ shows more variability than $\bar{u}$ is consistant with a pattern of waves traveling around the latitude circles.

The $\bar{v}$ fields show a high degree of vertical continuity when the three levels are compared and indicate good resolution of the vertical characteristics of the waves. A comparison of the long wave patterns with the continents supports the hypothesis that large land masses play a primary role in the production of the long waves.

It is interesting to note that there are many climatological charts of zonal flow available for many levels, but global charts of the time-averaged meridional flow are not readily available. More charts of this type will probably appear because of the relative ease of producing them from a global model such as this.

Longitude-and-time averaged values of u and v, which are defined by Equation (3.5) were computed using Equation (3.6).

$$x_o = \frac{1}{2\pi T} \int_0^{2\pi} \int_0^T x\,dT\,d\lambda \qquad (3.5)$$

$$x_o = \frac{1}{NM} \sum_{i=1}^{M} \sum_{j=1}^{N} (x_i)_j \qquad (3.6)$$

where λ = longitude,

$(x_i)_j = (u_i)_j$ or $(v_i)_j$,

$M = 70$ (number of time periods)

and $N = 72$ (number of longitudinal grid points).

Figure 13 is a vertical cross section for u_o. Values were computed at 200 mb, 500 mb, and 850 mb. The x's along these three axes represent the points where the isotach values occurred. The M's along the axes indicate points where relative positive maximums occurred, and the N's indicate where the largest absolute values of negative u_o's occurred. The results for v_o at the three levels are tabulated in Table 2.

Figure 13 agrees very closely with results obtained by Heastie and Stephenson (1960) for January 1958. There is a slight indication of both the polar jet and the subtropical jet at 500 mb in the Northern Hemisphere. In the Southern Hemisphere the only jet indicated is located about 48°S latitude.

The v_o values are generally smaller than those of Sadler, (1975), and Oort and Rasmusson (1971), for the tropical latitudes, but are comparable to those which may be inferred from Fig. 1 of Krishnamurti et al, (1973). There is good indication of the northern Hadley cell in the v_o field and also of the position of the ITCZ at about 20°S

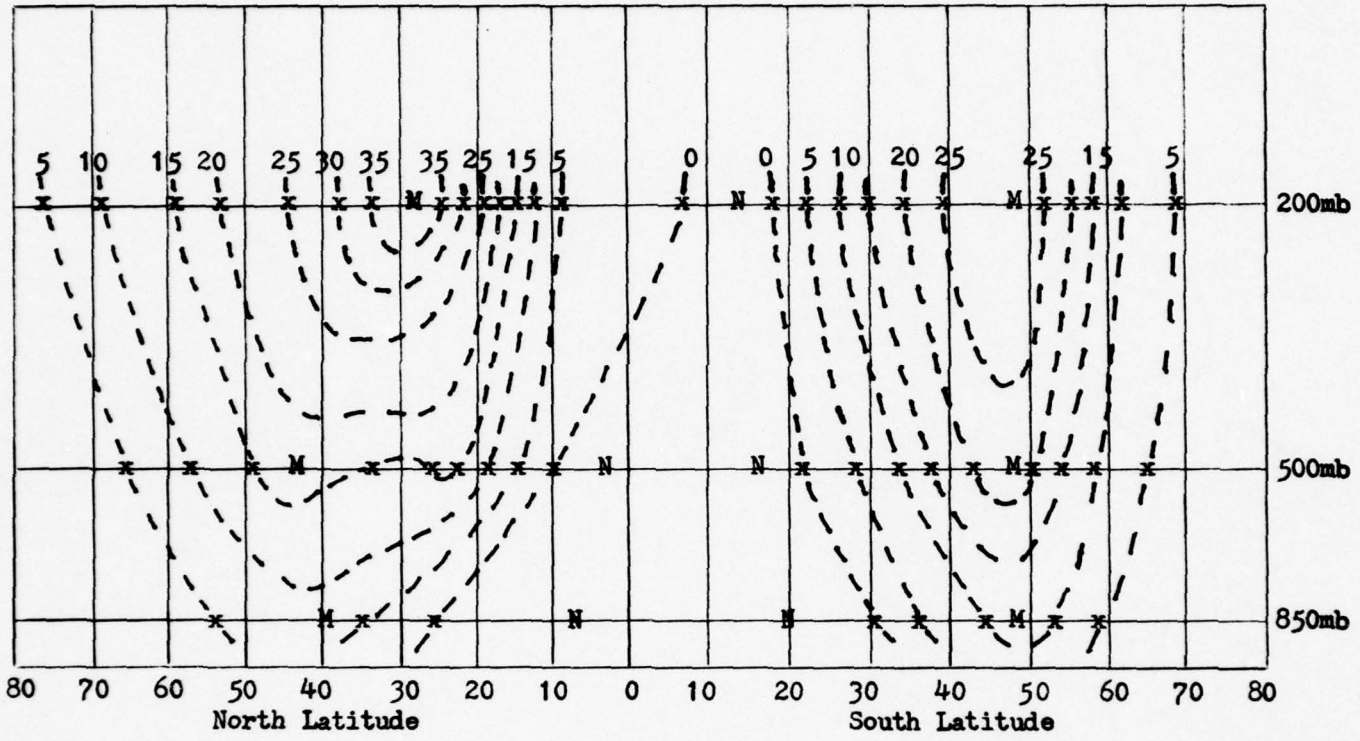

Figure 13 Vertical cross section of time-and-longitude averaged u wind component (m/sec).

TABLE 2

Time-and-Longitude Averaged v Wind Component

Latitude	850mb	500mb	200mb
84N	-.0	-.2	.1
80N	.1	-.3	-.0
76N	-.3	-.3	-.1
72N	-.3	-.1	-.5
68N	-.2	-.2	-.3
64N	-.2	-.2	-.3
60N	-.3	-.4	-.4
56N	.5	-.5	-.2
52N	.3	-.2	-.2
48N	.1	-.2	-.2
44N	.1	.0	-.3
40N	.2	.2	-.1
36N	.0	.1	-.0
32N	.2	.3	-.2
28N	.1	.2	-.0
24N	.0	.4	.8
20N	-.0	.3	1.2
16N	-.1	.4	1.6
12N	-.3	.6	1.3
8N	-.5	.7	1.4
4N	-.5	.3	1.0
0	-.8	.3	.7
4S	-1.0	-.3	.4
8S	-.7	-.3	.1
12S	-.6	-.3	.0
16S	-.5	-.2	-.2
20S	-.2	-.2	-.7
24S	-.1	-.2	-.4
28S	.0	-.1	-.4
32S	.0	.0	.1
36S	.1	-.0	.1
40S	.1	-.1	-.3
44S	-.1	.1	-.3
48S	-.0	.1	.0
52S	-.1	.1	.1
56S	-.1	.1	-.0
60S	.0	-.1	-.2
64S	-.1	-.2	-.2
68S	-.2	-.1	-.2
72S	-.2	-.0	-.2
76S	.1	-.1	-.1
80S	-.2	.0	-.0
84S	.0	.1	-.0

Units are m/sec

at 850 mb. It also appears that an equator-ward slope with height is detectable for the ITCZ.

Time-Averaged Kinetic Energy Fields

The standing kinetic energy per unit mass (SKE) at each point is defined as:

$$SKE = \frac{\overline{u}^2 + \overline{v}^2}{2} . \qquad (3.8)$$

SKE fields for the three levels were computed from the time-averaged wind fields. Figures 14 and 15 are the 200 mb SKE fields for the Northern and Southern Hemispheres respectively. Figures 16, 17, 18 and 19 are the corresponding fields for 500 mb and 850 mb.

These charts show the average jet stream positions. Three distinct jets are detectable in the Northern Hemisphere in mid-latitudes at 200 mb and 500 mb. One along the East Coast of the United States, one over northern African and the Middle East, and the strongest one off the coast of Asia. At 850 mb there are only two wind maxima, the one off the East Coast of the United States, which is the strongest, and the one off the coast of Asia. The 500 mb chart shows some indication of the flow splitting and going around the Tibetian high country. The locations of the jet cores are in good agreement with climatological charts for January and February, (Namias, 1963), (Sadler, 1975).

In the Southern Hemisphere only one mid-latitude jet is detectable but it appears at all three levels. This jet is centered along the 48° S latitude line and runs west to east. This is in constrast to the Northern Hemisphere jets which are oriented from southwest to northeast. The position of this jet core, centered about 48° S latitude and between

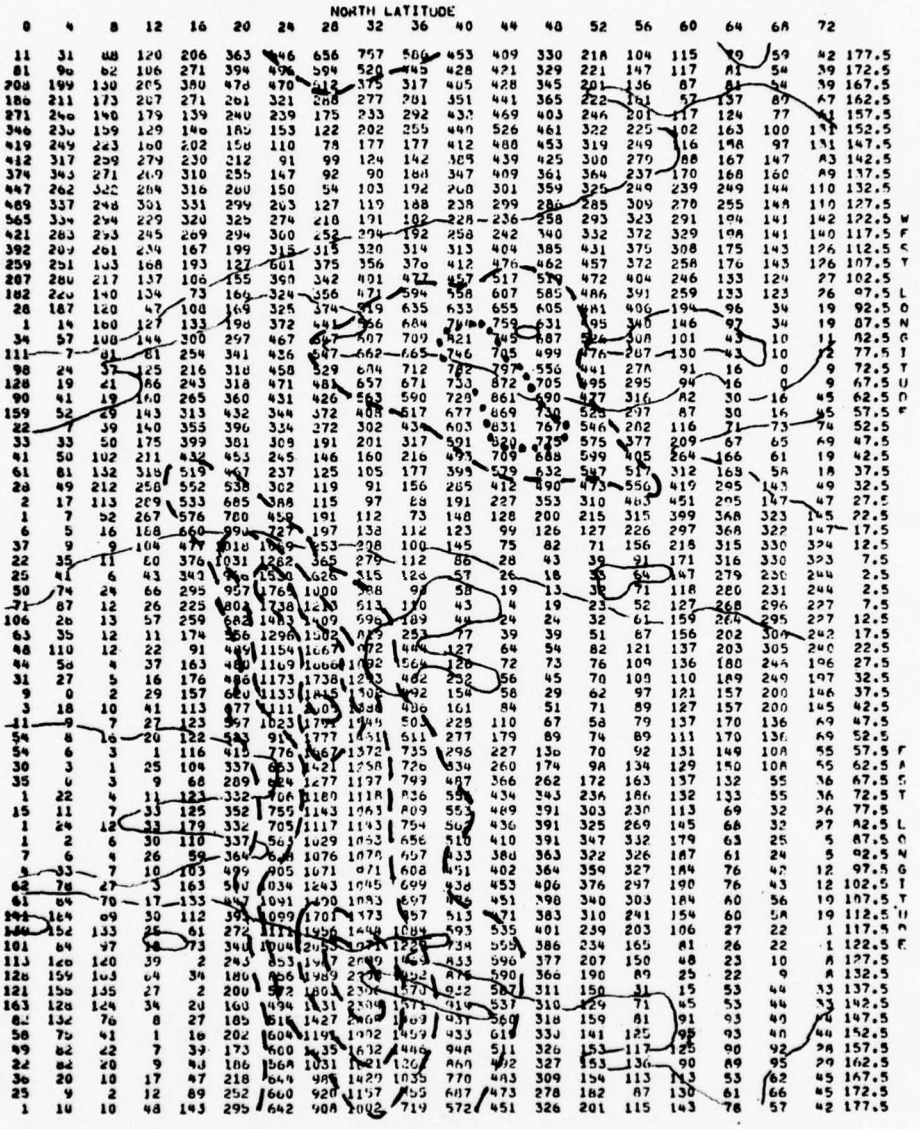

Figure 14 Standing kinetic energy per unit mass for N.H. at 200 mb (m^2/sec^2); dashed isolines are for values of 500, 1000, 1500 and 2000; dotted isoline denotes a value of 750.

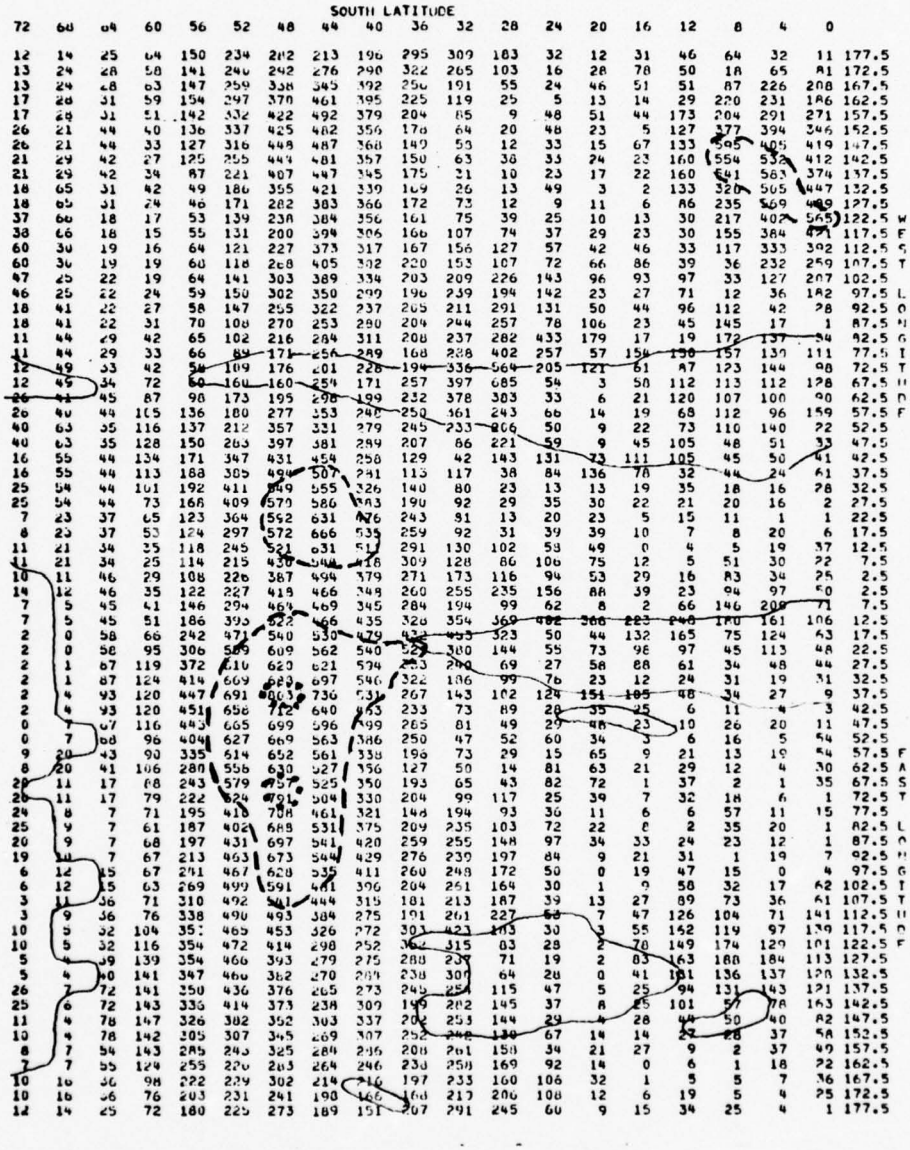

Figure 15 Standing kinetic energy per unit mass for S.H. at 200 mb (m^2/sec^2); dashed isolines are for a value of 500, dotted isolines denote 750 values.

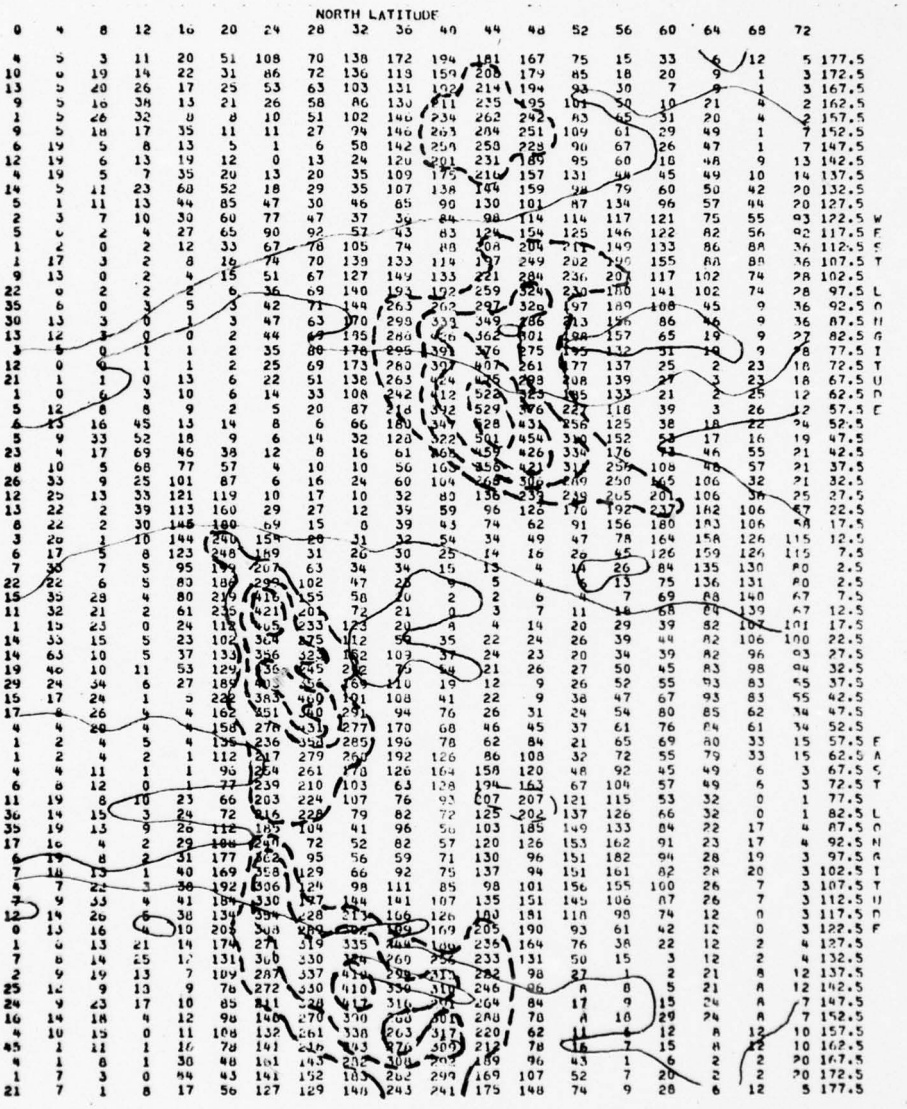

Figure 16 Standing kinetic energy per unit mass for N.H. at 500 mb (m^2/sec^2); dashed isolines are for values of 200, 300, 400 and 500.

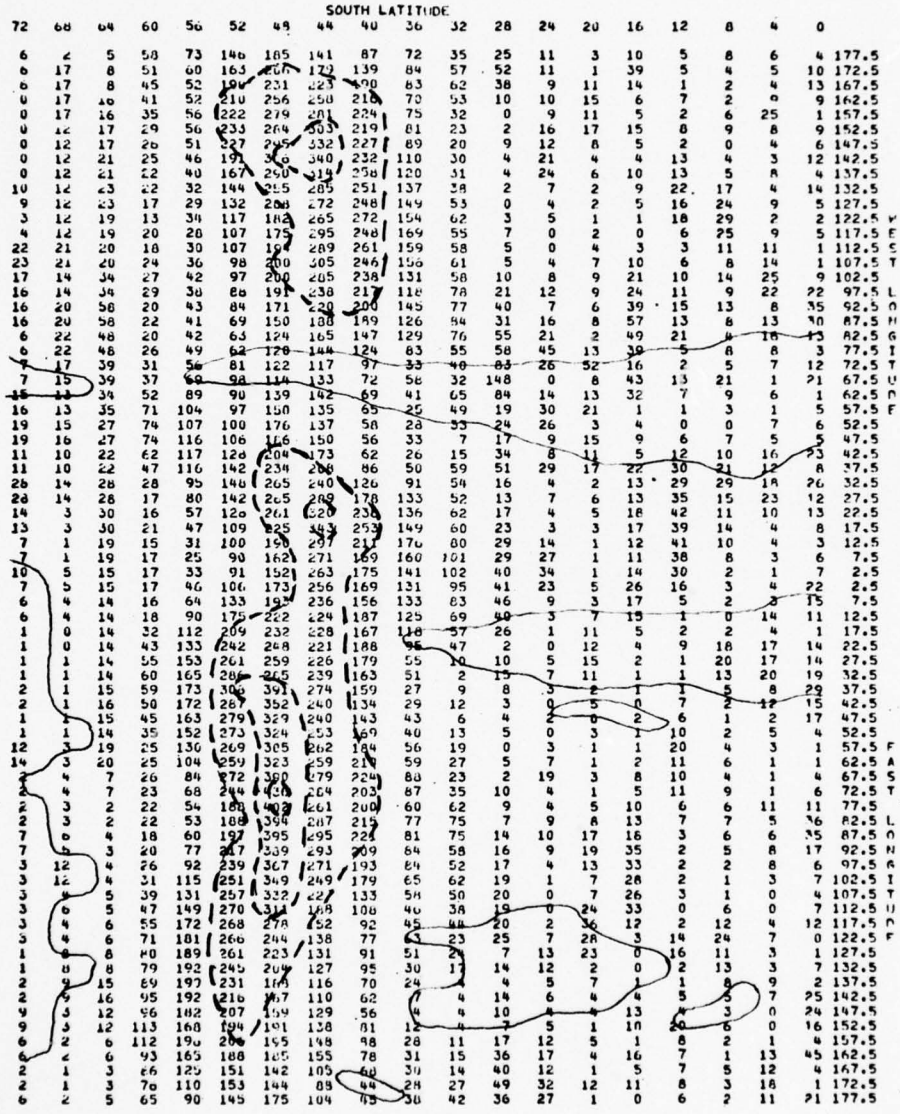

Figure 17 Standing kinetic energy per unit mass for S.H. at 500 mb (m^2/sec^2); dashed isolines are for values of 200, 300 and 400.

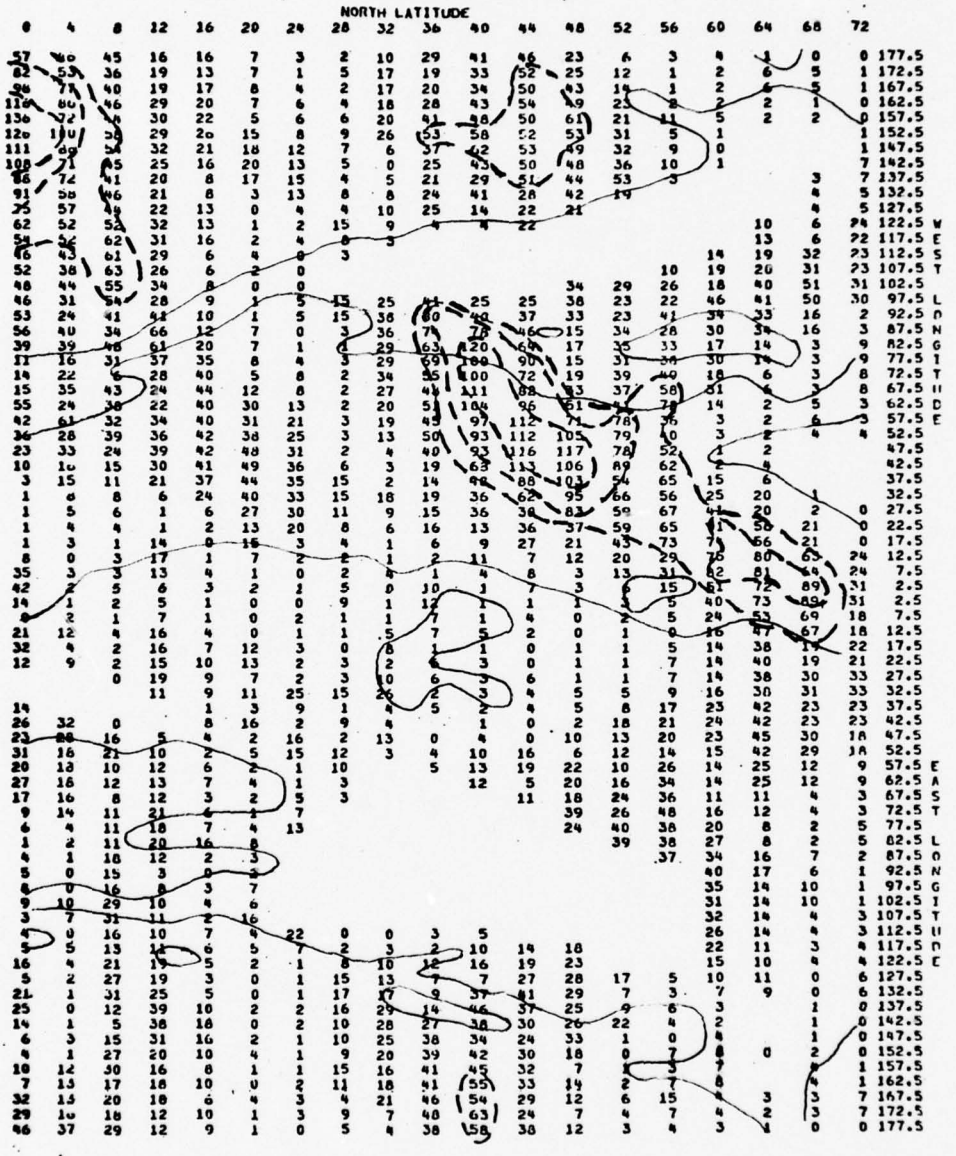

Figure 18 Standing kinetic energy per unit mass for N.H. at 850 mb (m^2/sec^2); dashed isolines are for values of 50, 75 and 100; areas where 850 mb surface is below ground are blank.

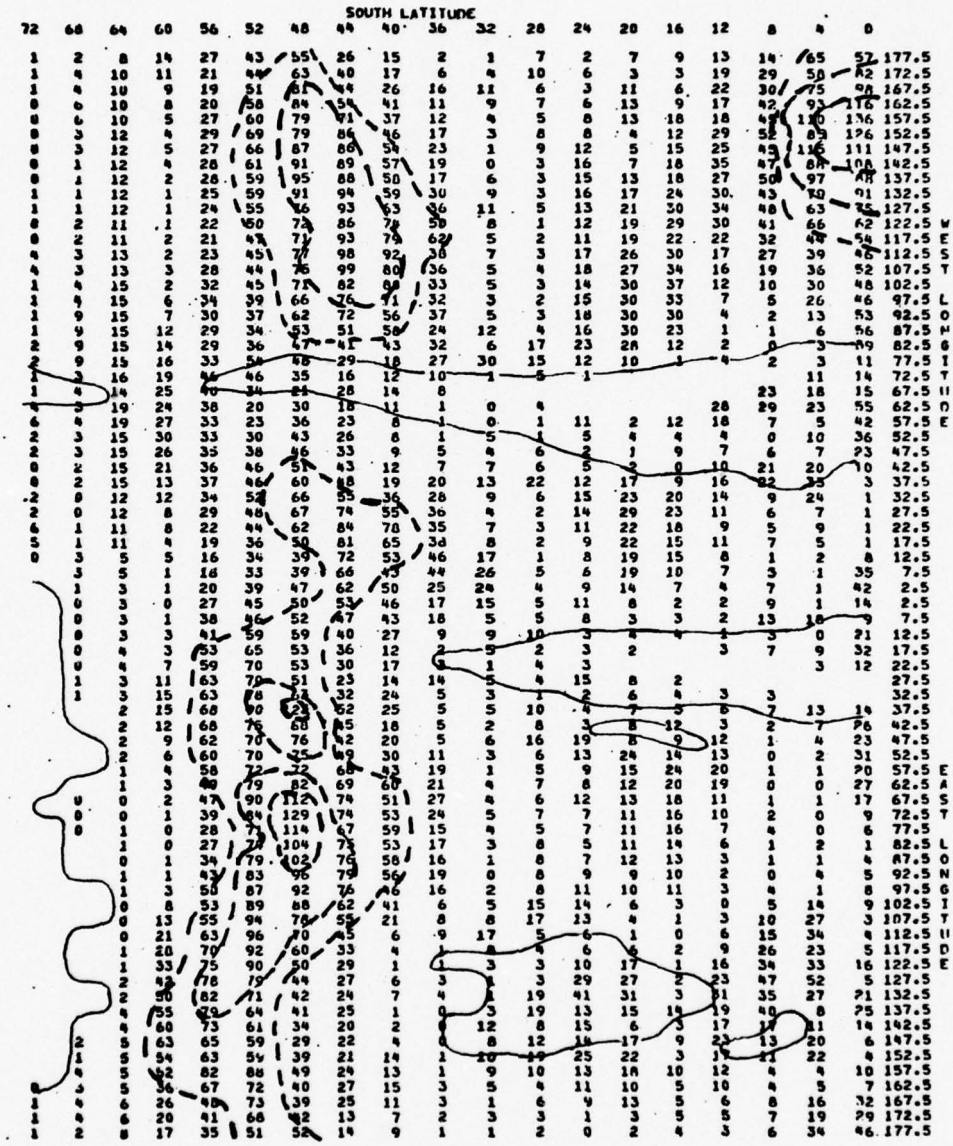

Figure 19 Standing kinetic energy per unit mass for S.H. at 850 mb (m^2/sec^2); dashed isolines are for values of 50, 75, and 100; areas where 850 mb surface is below ground are blank.

37° E and 78° E longitude is also in agreement with other similar analyses, (van Loon, 1971).

In the tropical Pacific area, the westerly jet at 200 mb, which crosses the equator is of interest. The core is at 4° S latitude and the wind speeds are considerably stronger than the February average given by Sadler, (1975). He shows about 45 knots as the maximum where this data has an area with wind speeds of near 60 knots with the maximum about 65 knots. An examination of the $\overline{u}$, $\overline{v}$ and steady energy charts for 200 mb reveals a large Pacific trough associated with this jet.

Equation (3.8) defines the time-averaged transient kinetic energy ($\overline{TKE}$) per unit mass as

$$\overline{TKE} = \frac{1}{T} \int_0^T \frac{u^{*2} + v^{*2}}{2} dt \qquad (3.8)$$

with $u^* = u - \overline{u}$ and $v^* = v - \overline{v}$.

The $\overline{TKE}$ was computed directly from the standard deviation fields of the time-averaged wind components as follows:

$$\overline{SDX}^2 = \frac{1}{N} \sum_{i=1}^{N} (x_i - \overline{x})^2 \qquad (3.9)$$

$$x_i = u_i \text{ or } v_i \text{ and } N = 70.$$

$$\overline{TKE} = \frac{\overline{SDU}^2 + \overline{SDV}^2}{2} \qquad (3.10)$$

where $\overline{SDU}$ and $\overline{SDV}$ are the standard deviations of $\overline{u}$ and $\overline{v}$ respectively. These fields are depicted in Figures 20, 21, 22, 23, 24 and 25.

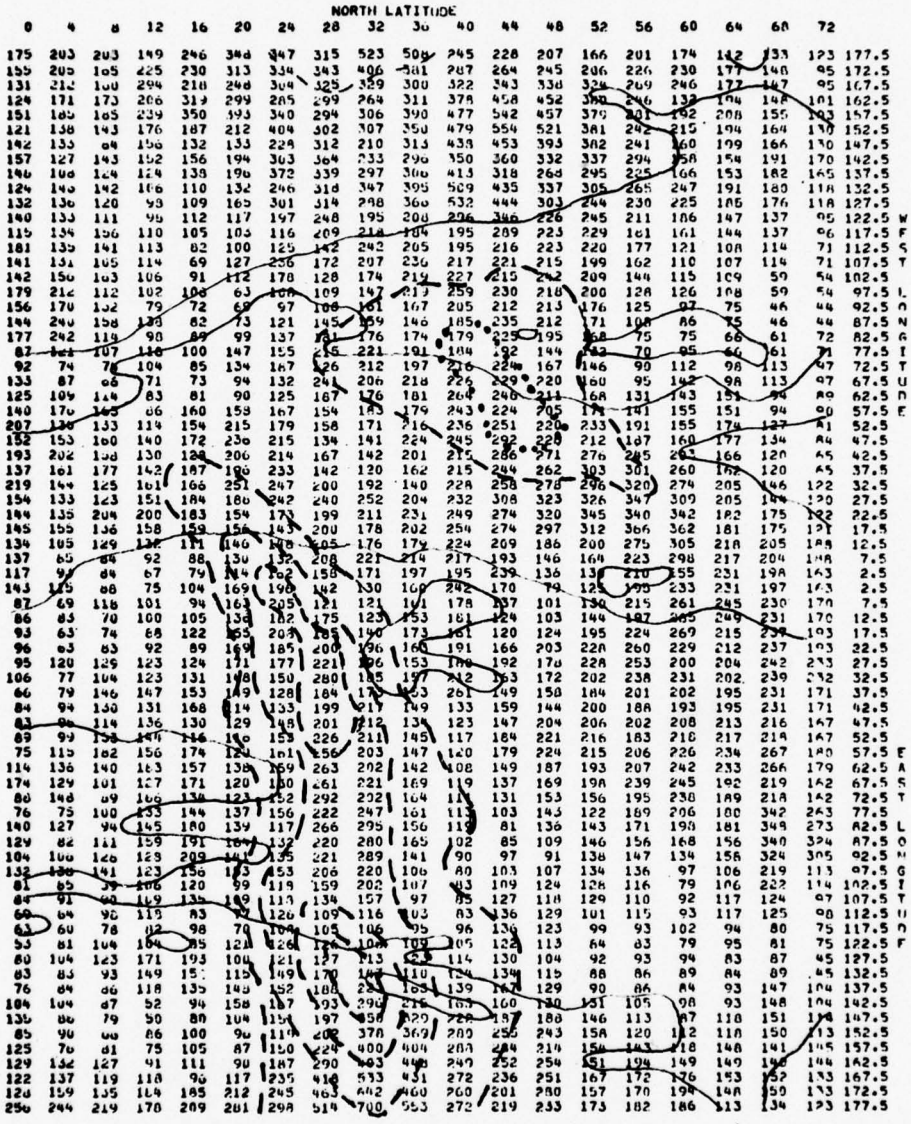

Figure 20 Time-averaged transient kinetic energy per unit mass for N.H. at 200 mb (m^2/sec^2); isolines are for SKE and are from Figure 14.

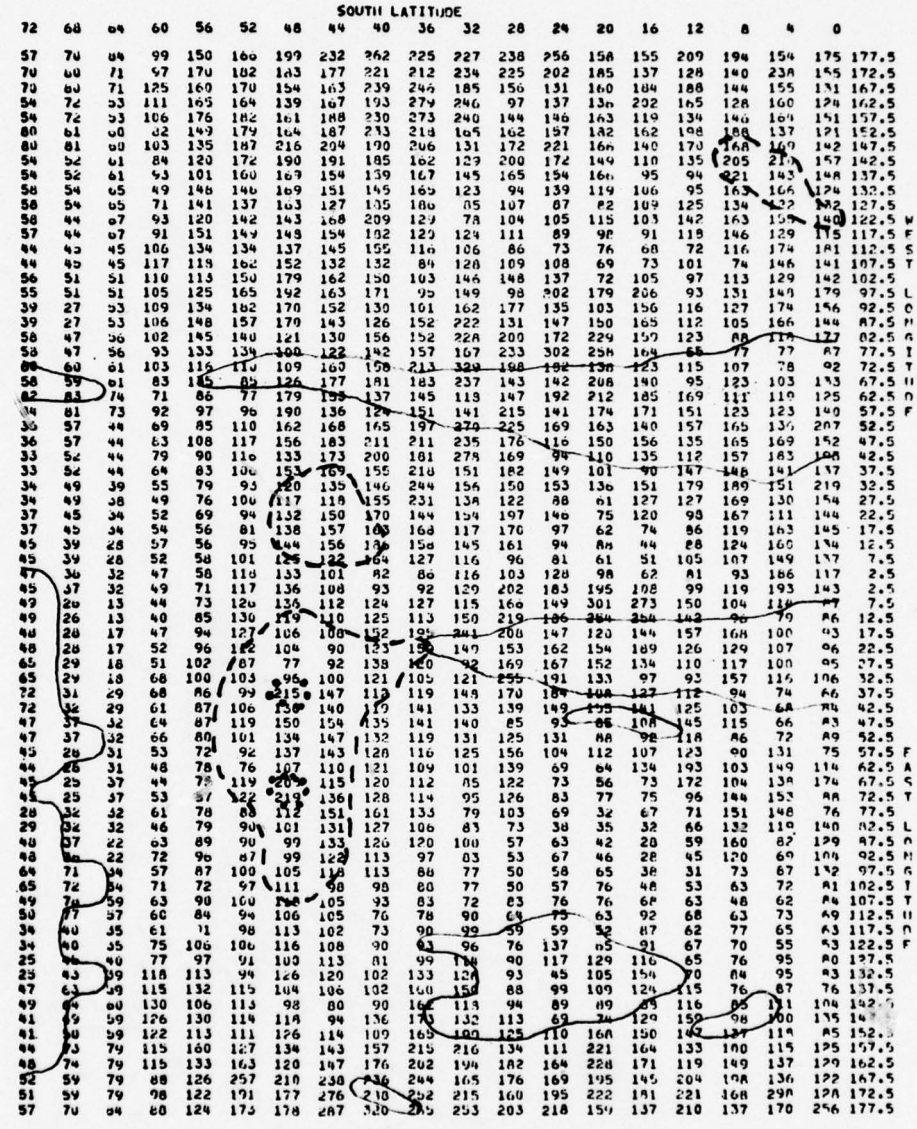

Figure 21 Time-averaged transient kinetic energy per unit mass for S.H. at 200 mb (m^2/sec^2); isolines are for SKE and are from Figure 15.

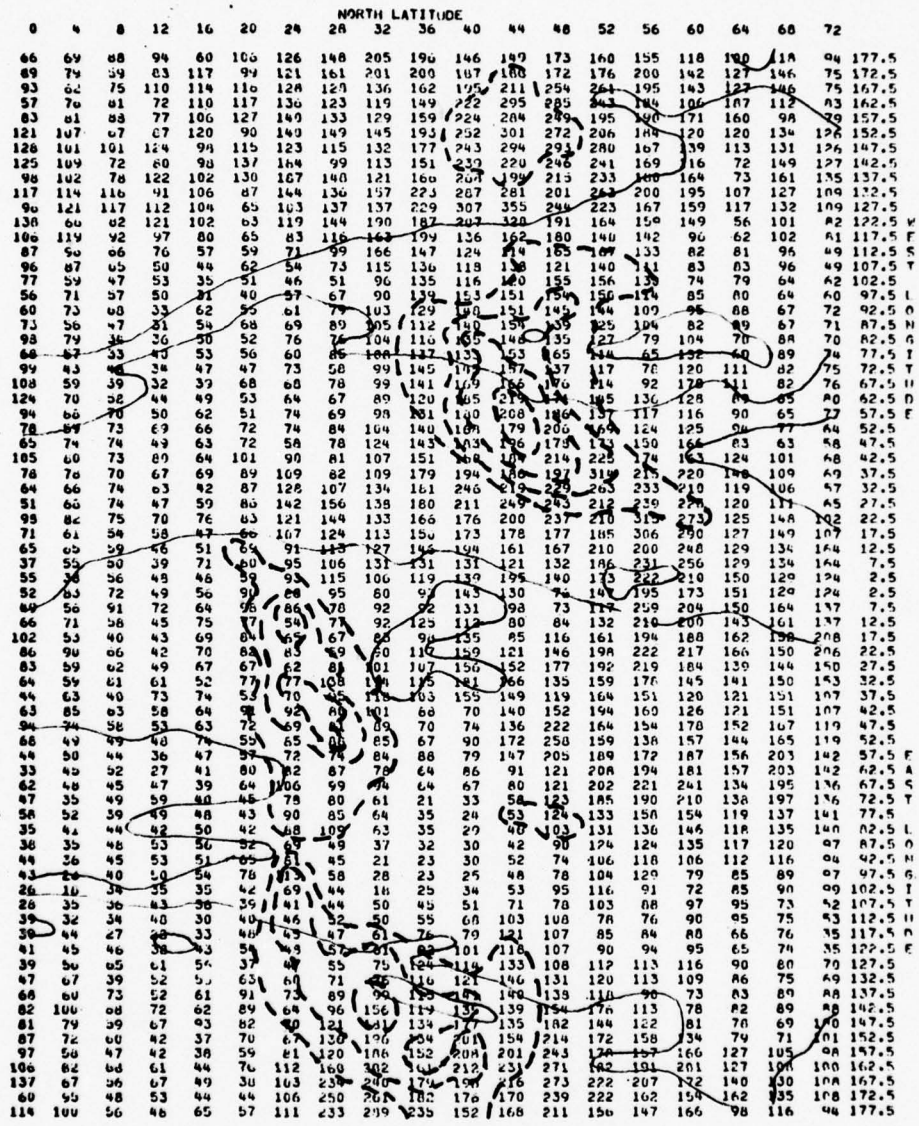

Figure 22 Time-averaged transient kinetic energy per unit mass for N.H. at 500 mb (m^2/sec^2); isolines are for SKE and are from Figure 16.

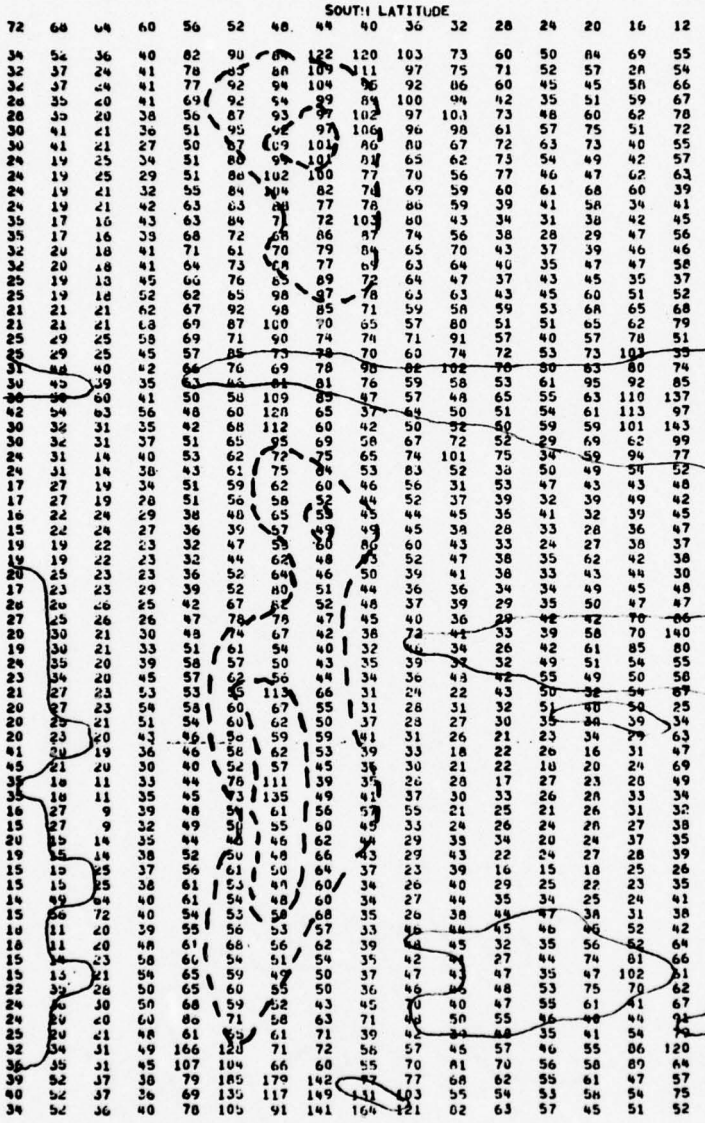

Figure 23 Time-averaged transient kinetic energy per unit mass for S.H. at 500 mb (m^2/sec^2); isolines are for SKE and are from Figure 17.

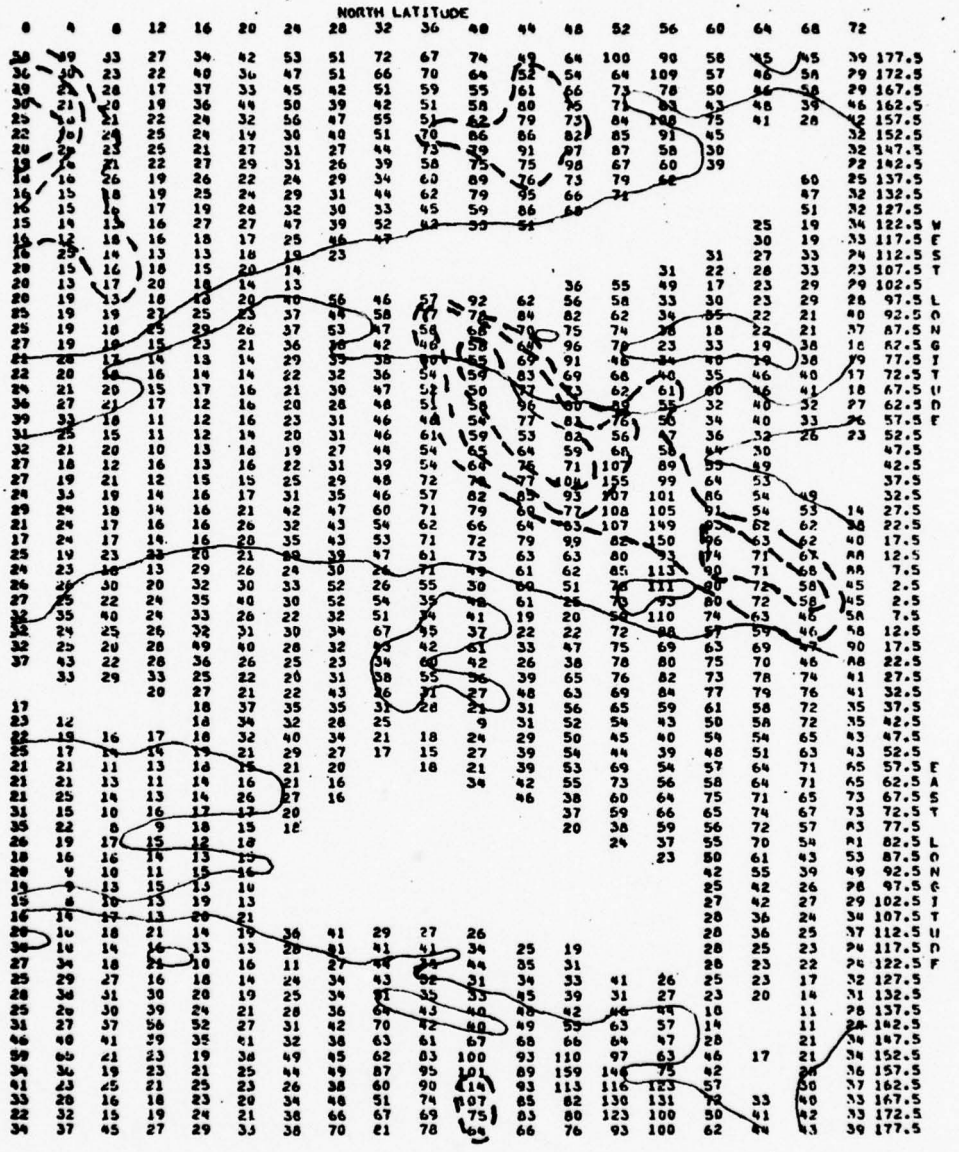

Figure 24 Time-averaged transient kinetic energy per unit mass for N.H. at 850 mb (m^2/sec^2); isolines are for SKE and are from Figure 18; areas where 850 mb surface is below ground are blank.

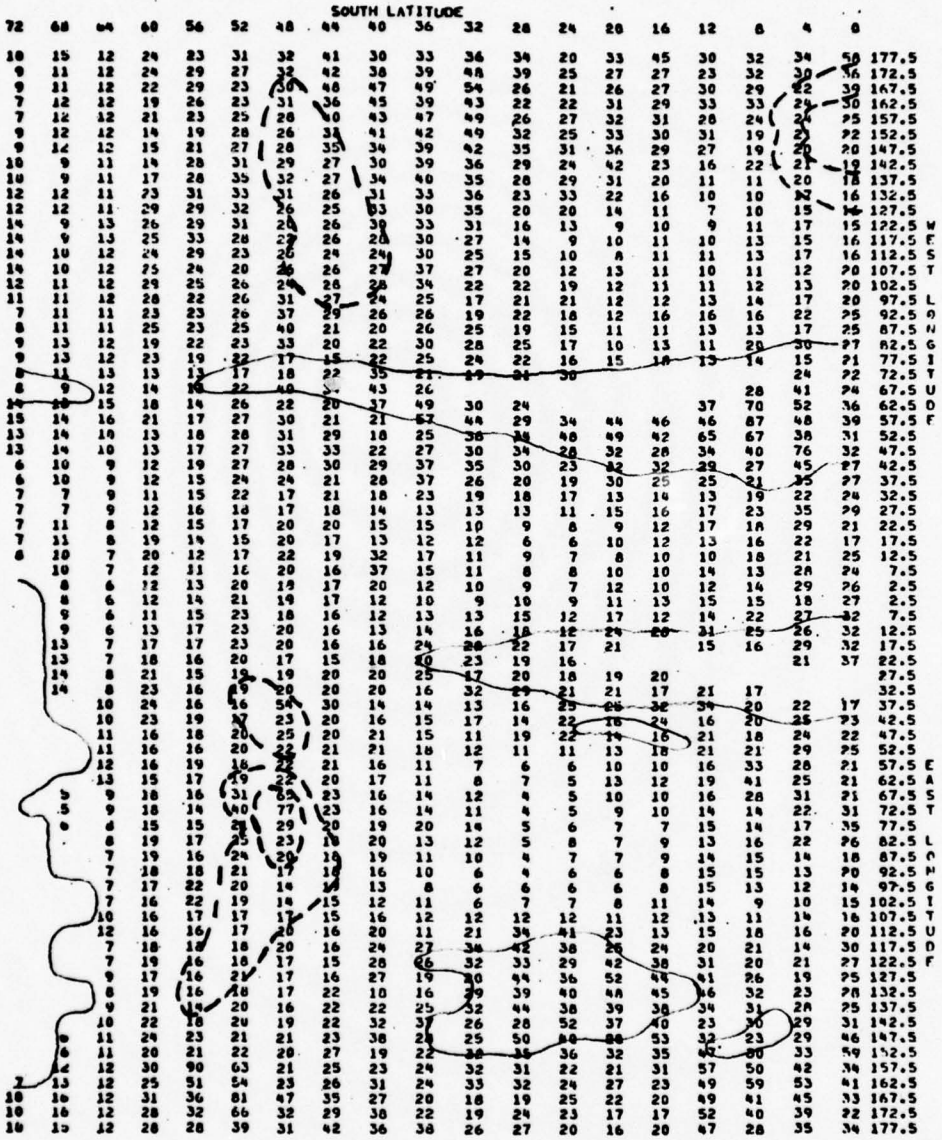

Figure 25 Time-averaged transient kinetic energy per unit mass for S.H. at 850 mb (m^2/sec^2); isolines are for SKE and are from Figure 19; areas where 850 mb surface is below ground are blank.

The isotachs from the corresponding standing kinetic energy charts are included on the $\overline{TKE}$ fields. This makes it possible to compare the transient energy with the average position of the wind maxima.

By using the $\bar{u}$ charts it is possible to compare the transient energy on the upwind and downwind sides of mountains in several locations. By following along the 44° N latitude circle it is possible to detect a drop in the transient energy to the east of the Rockies and the Himalayas. This suggests that the mountains are responsible for deflecting the transient eddies.

Time-Averaged Divergence and Relative Vorticity Fields

Divergence and relative vorticity fields were produced from the time-averaged wind fields. In spherical coordinates, the horizontal divergence and vorticity along a constant pressure surface are given by

$$DIV = \frac{1}{a \cos \phi} \frac{\partial u}{\partial \lambda} + \frac{1}{a} \frac{\partial v}{\partial \phi} - \frac{v \tan \phi}{a} \qquad (3.11)$$

and

$$VOR = \frac{1}{a \cos \phi} \frac{\partial v}{\partial \lambda} - \frac{1}{a} \frac{\partial u}{\partial \phi} + \frac{u \tan \phi}{a} \qquad (3.12)$$

where a is the radius of the earth, λ is longitude and ϕ is latitude.

To compute the divergence and the vorticity, Equations (3.11) and (3.12) were put into the following finite-difference form:

$$DIV_{i,j} = \frac{1}{a} \left[\frac{u_{i+1,j} - u_{i-1,j}}{\Delta\lambda \cos \phi_j} + \frac{v_{i,j+1} - v_{i,j-1}}{\Delta\phi} - v_{ij} \tan \phi_j \right] \qquad (3.13)$$

$$VOR_{i,j} = \frac{1}{a}\left[\frac{v_{i+1,j} - v_{i-1,j}}{\Delta\lambda \cos \phi_j} - \frac{u_{i,j+1} - u_{i,j-1}}{\Delta\phi} + u_{ij} \tan \phi_j\right].$$

(3.14)

Centered space differencing was used to approximate the derivatives.

To aid in the identification of clusters, these fields were output in two parts. One part has the negative values blanked out and the other omits the positive values. The positive, time-averaged divergence fields are contained in Figures 26 , 27 and 28. Figures 29 , 30 and 31 show the corresponding negative divergences. Positive time-averaged vorticities for 500 mb are in Figure 32, while Figure 33 has the negative values. The vorticity charts at 200 mb and 850 mb showed similar patterns so they were not included. It should be noted that positive relative vorticities correspond to cyclonic vorticity in the Northern Hemisphere and anticyclonic vorticities in the Southern Hemisphere. Standard deviations for the above charts were calculated using Equation (3.4) with X_i replaced by the divergence or the relative vorticity. Figures 34 and 35 are the standard deviations of the time-averaged divergences and vorticity fields at 500 mb.

A comparison of the time-averaged divergence fields with their standard deviations shows that the standard deviations are generally larger than the time-averaged divergences. At some points the standard deviations are an order of magnitude larger. This suggests that the time-averages are small numbers resulting from oscillations between

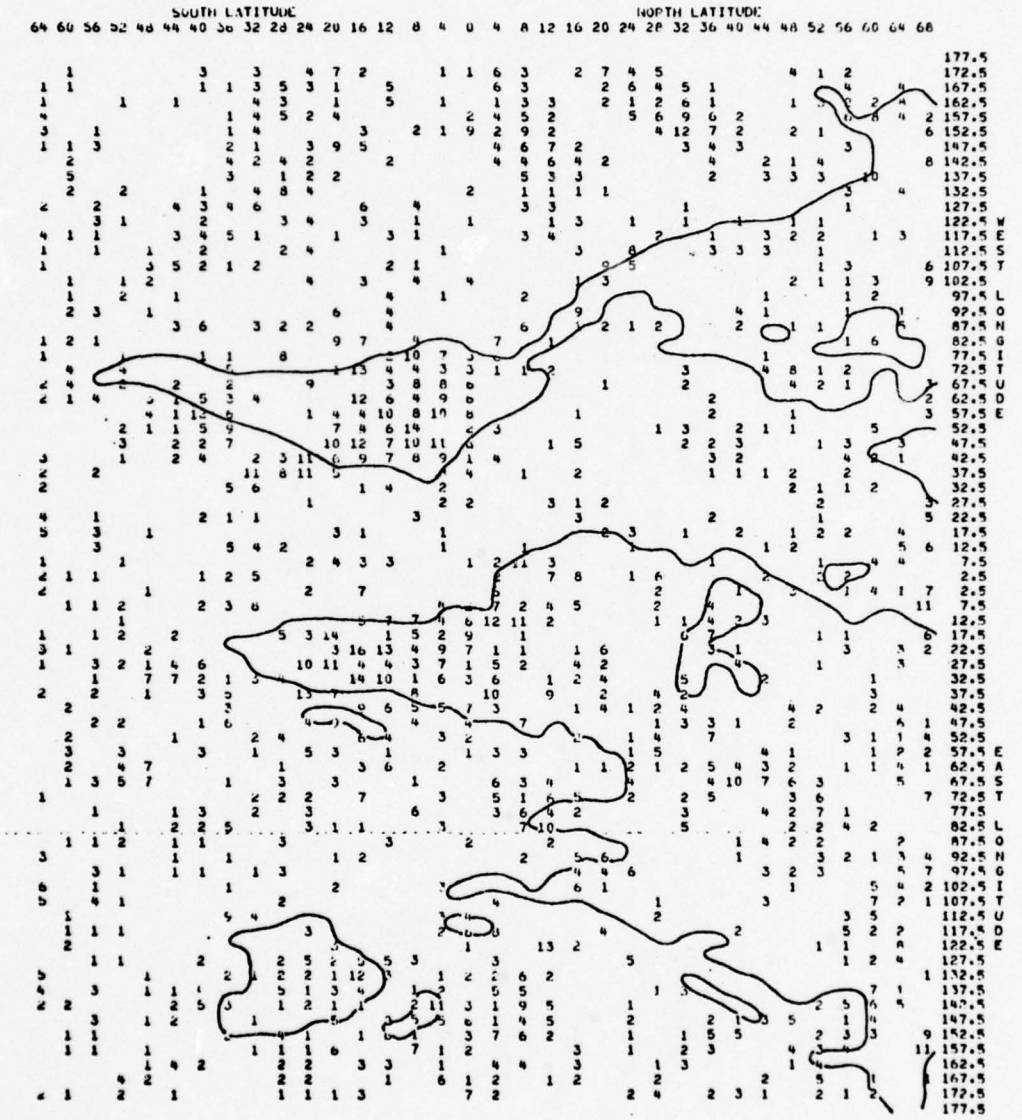

Figure 26 Positive time-averaged divergence at 200 mb ($x10^{-6}sec^{-1}$).

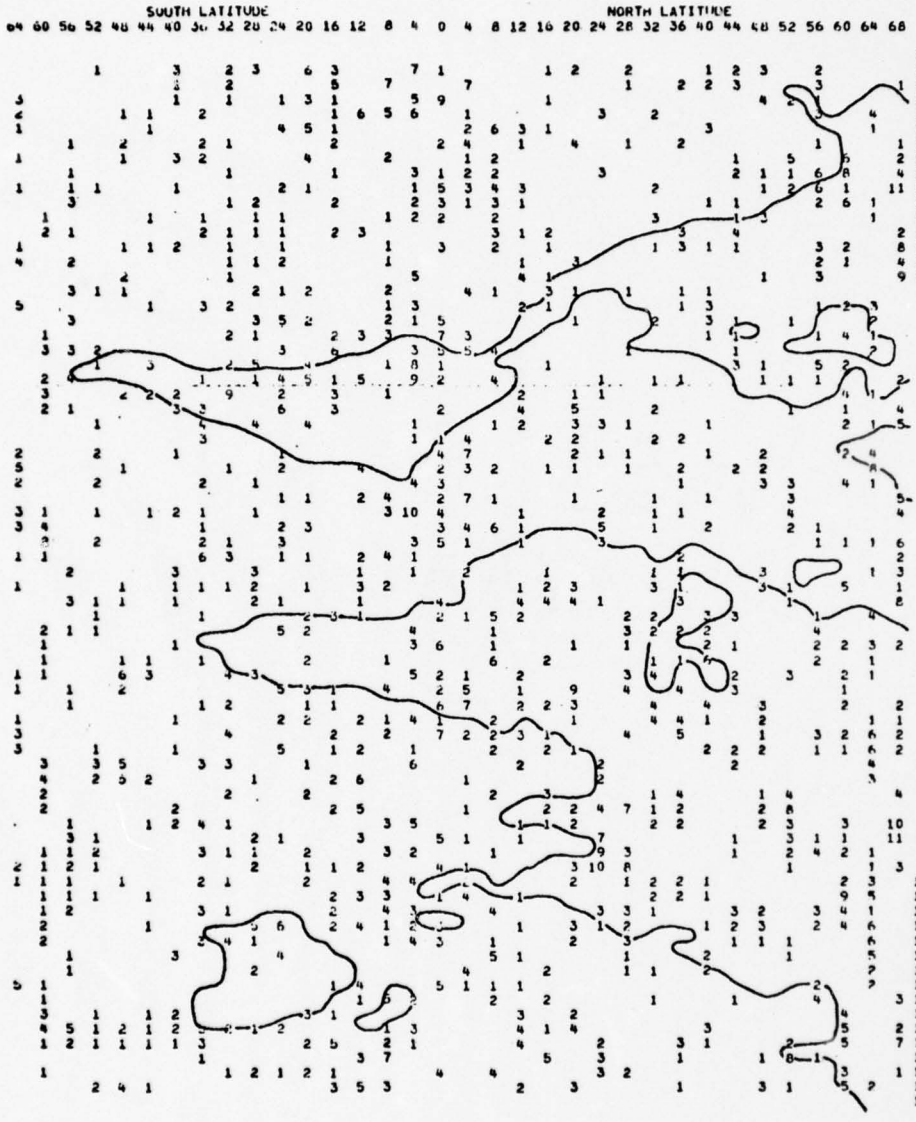

Figure 27 Positive time-averaged divergence at 500 mb ($x10^{-6}sec^{-1}$).

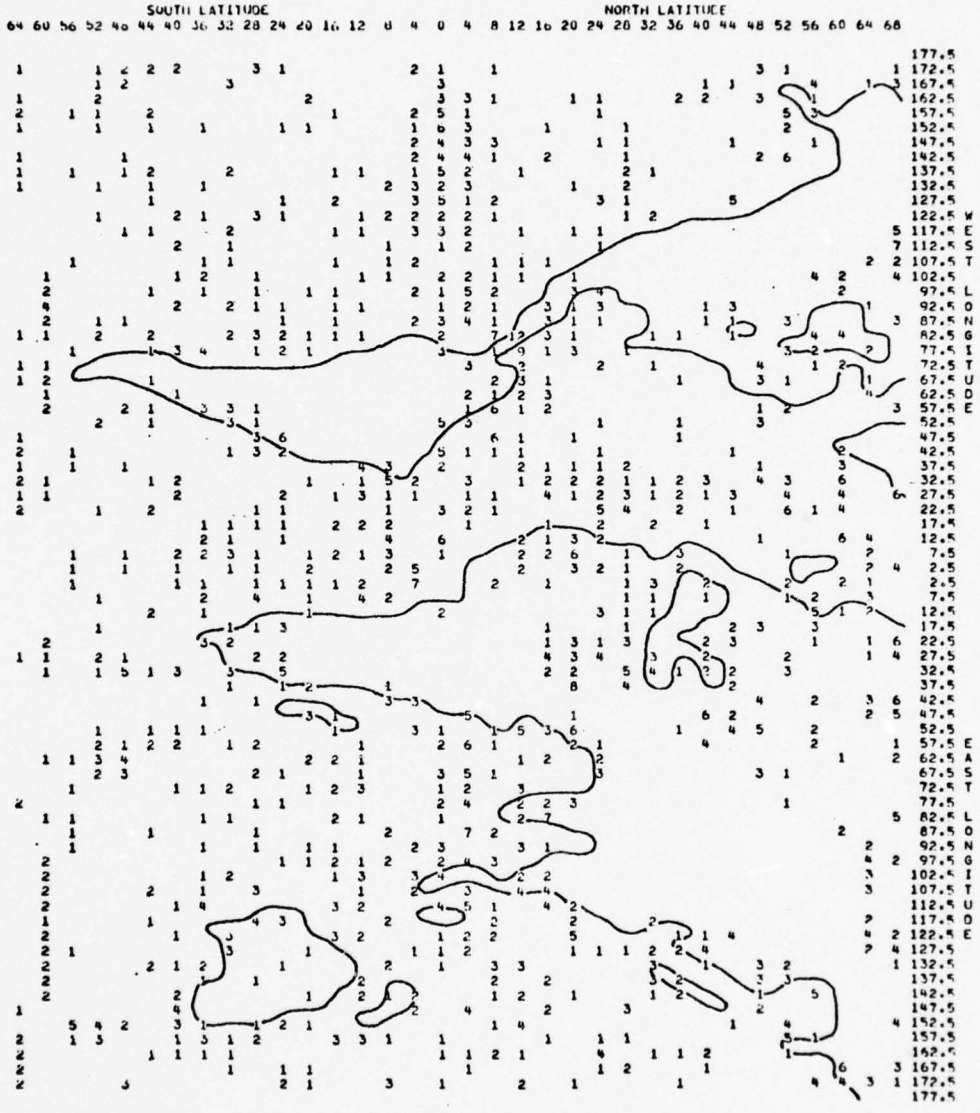

Figure 28 Positive time-averaged divergence at 850 mb ($x10^{-6}sec^{-1}$).

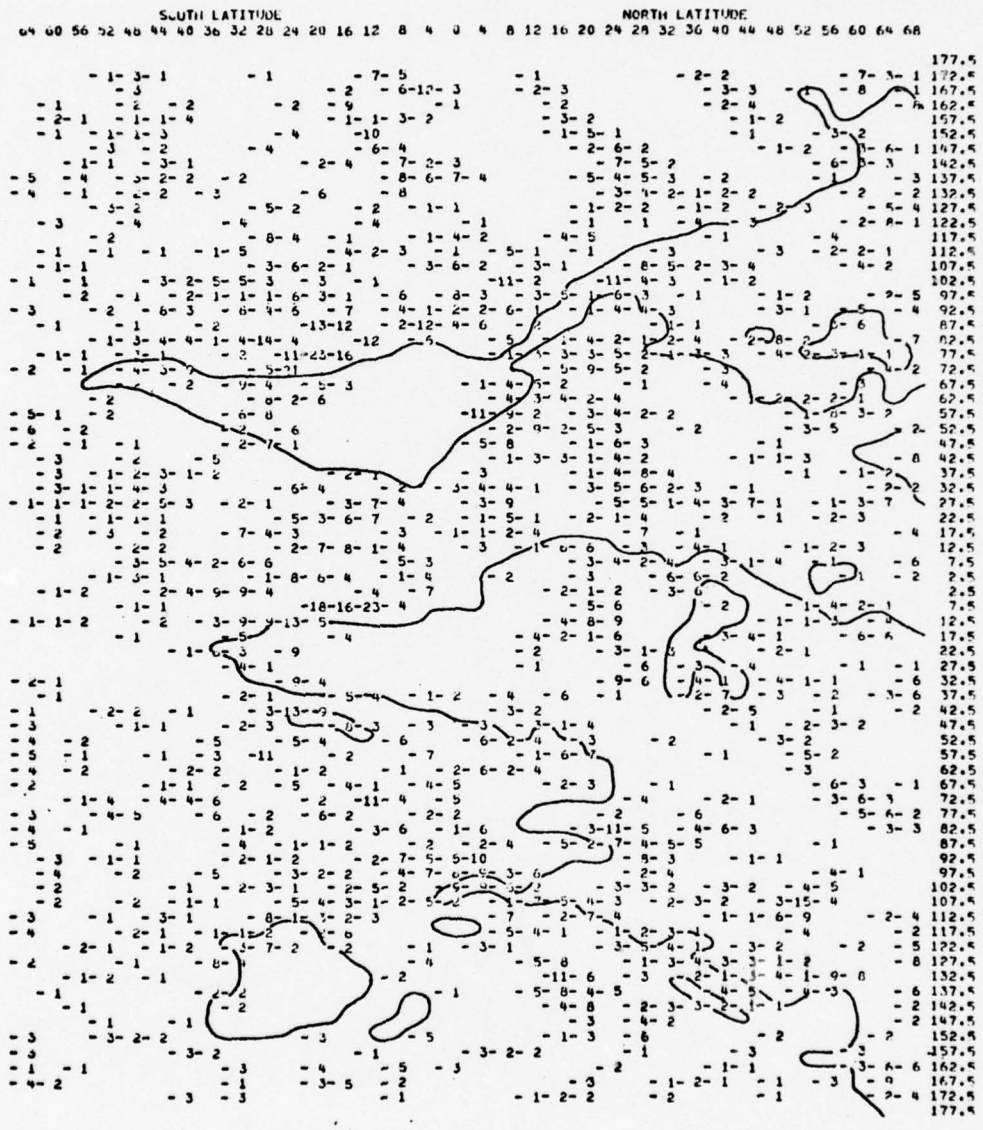

Figure 29 Negative time-averaged divergence at 200 mb ($x10^{-6}sec^{-1}$).

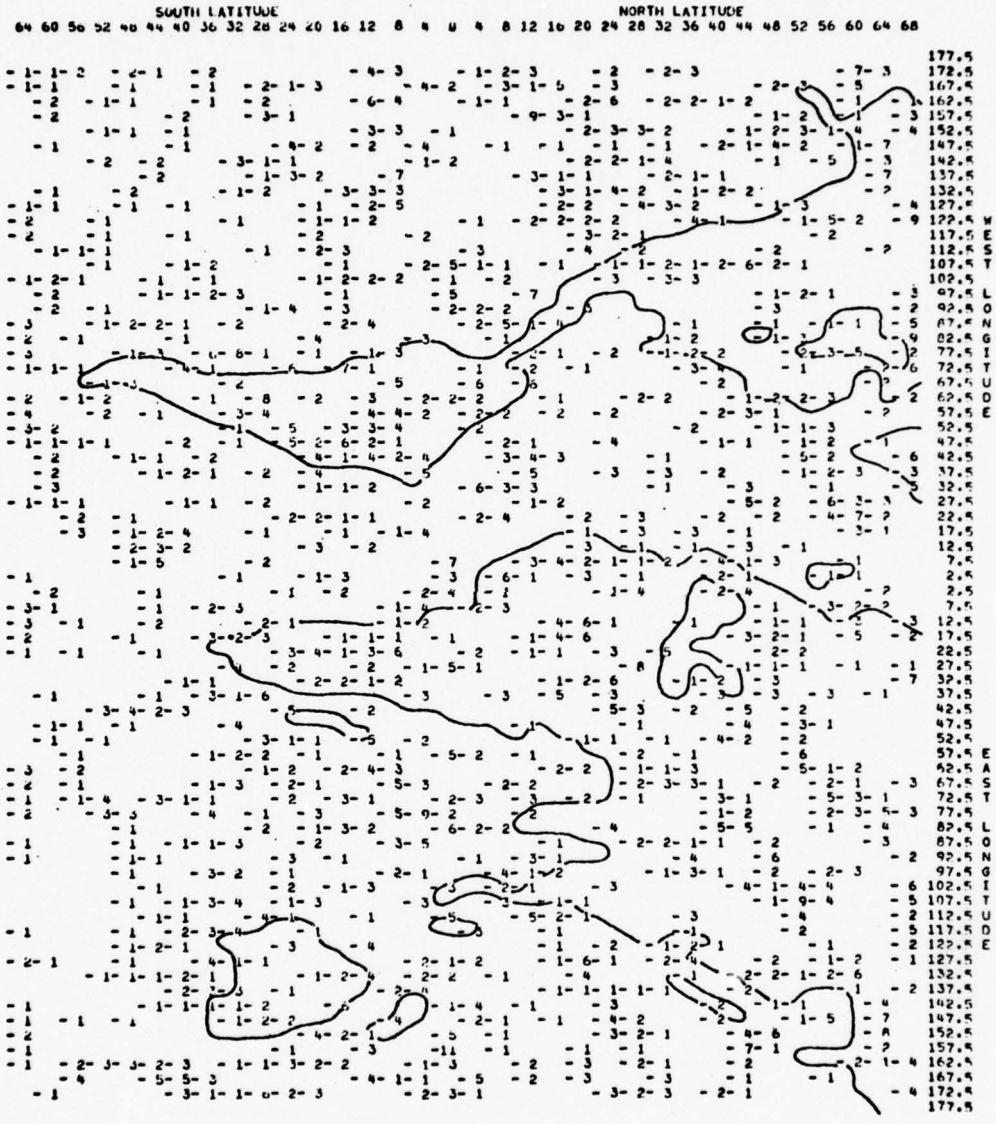

Figure 30 Negative time-averaged divergence at 500 mb ($x10^{-6}sec^{-1}$).

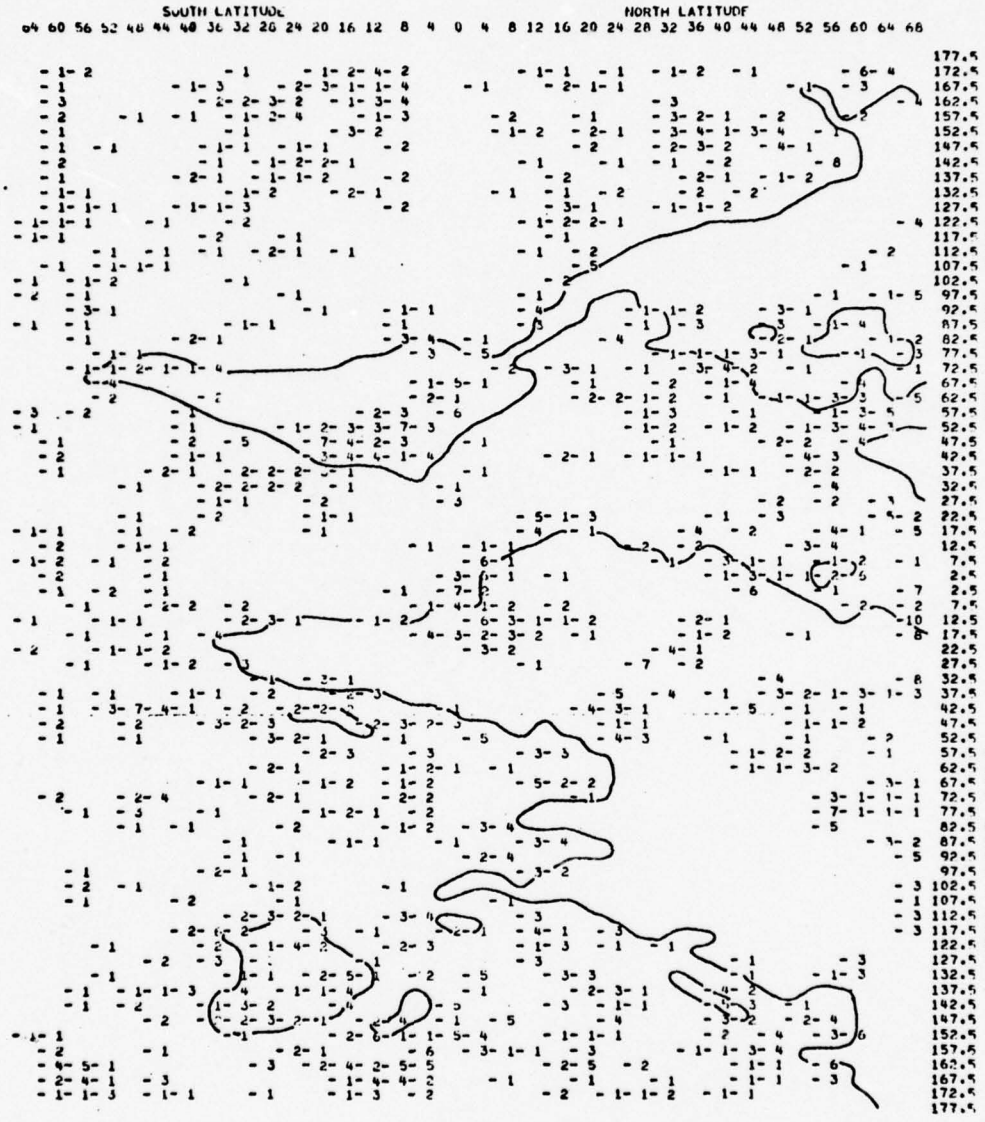

Figure 31 Negative time-averaged divergence at 850 mb ($x10^{-6}sec^{-1}$).

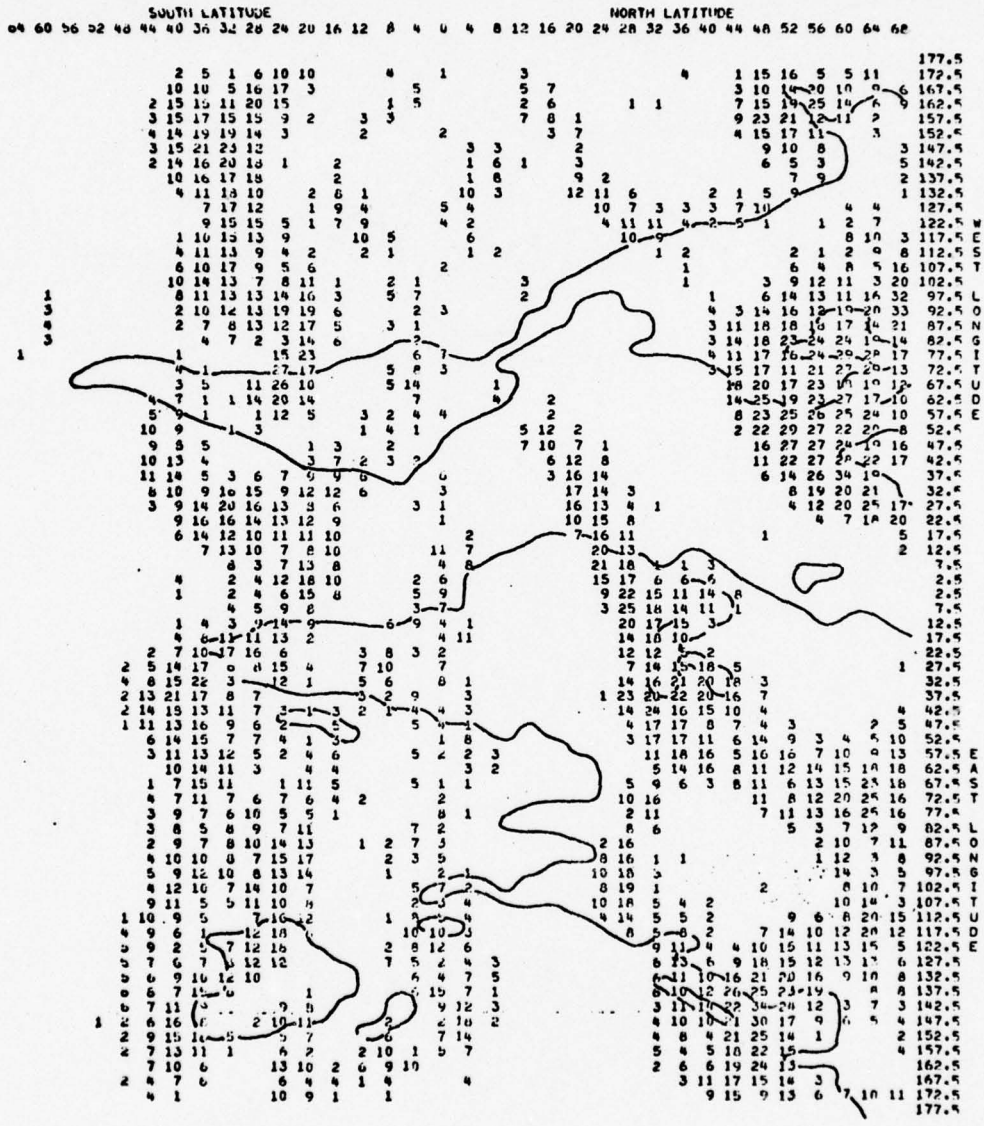

Figure 32 Positive time-averaged relative vorticity at 500 mb ($x10^{-6}sec^{-1}$).

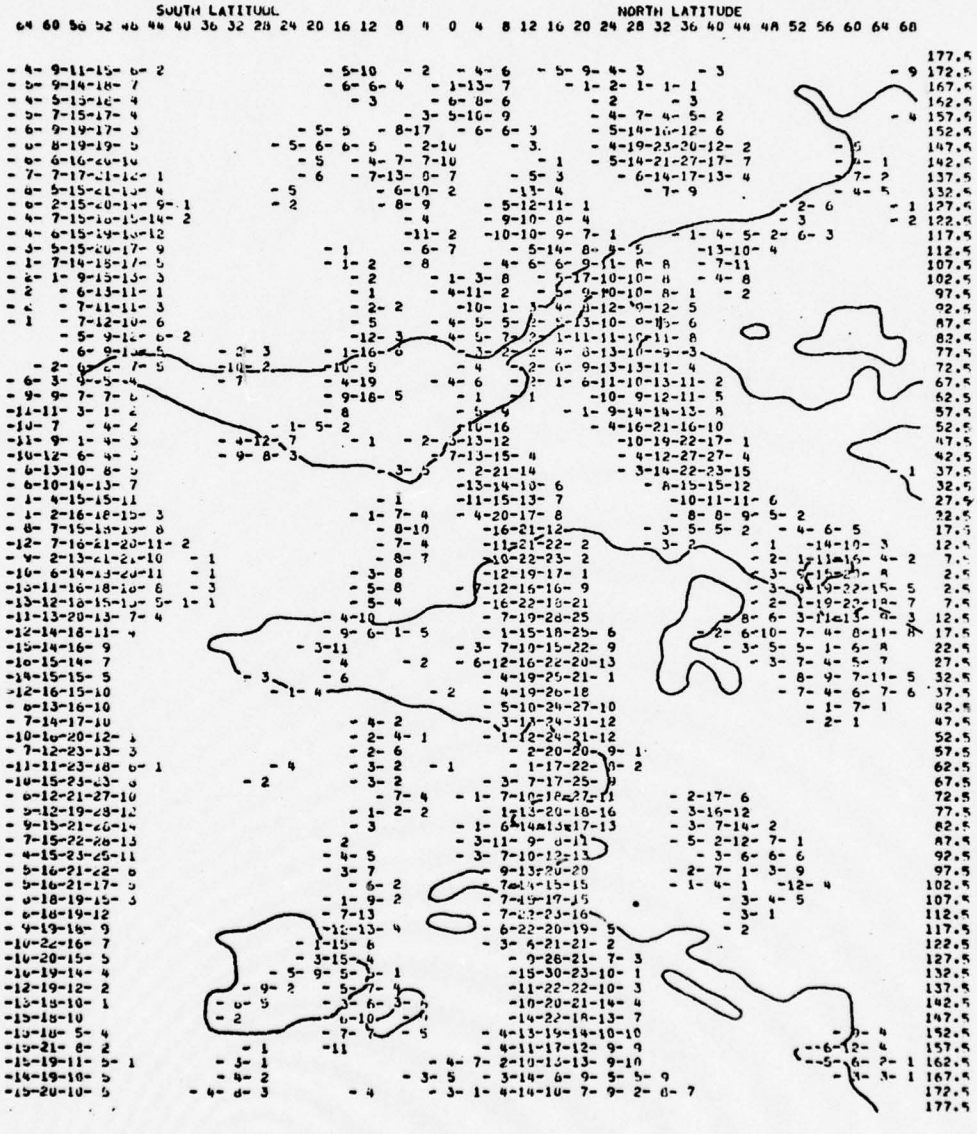

Figure 33 Negati[illegible] time-averaged relative vorticity at 500 mb (x10-[illegible]).

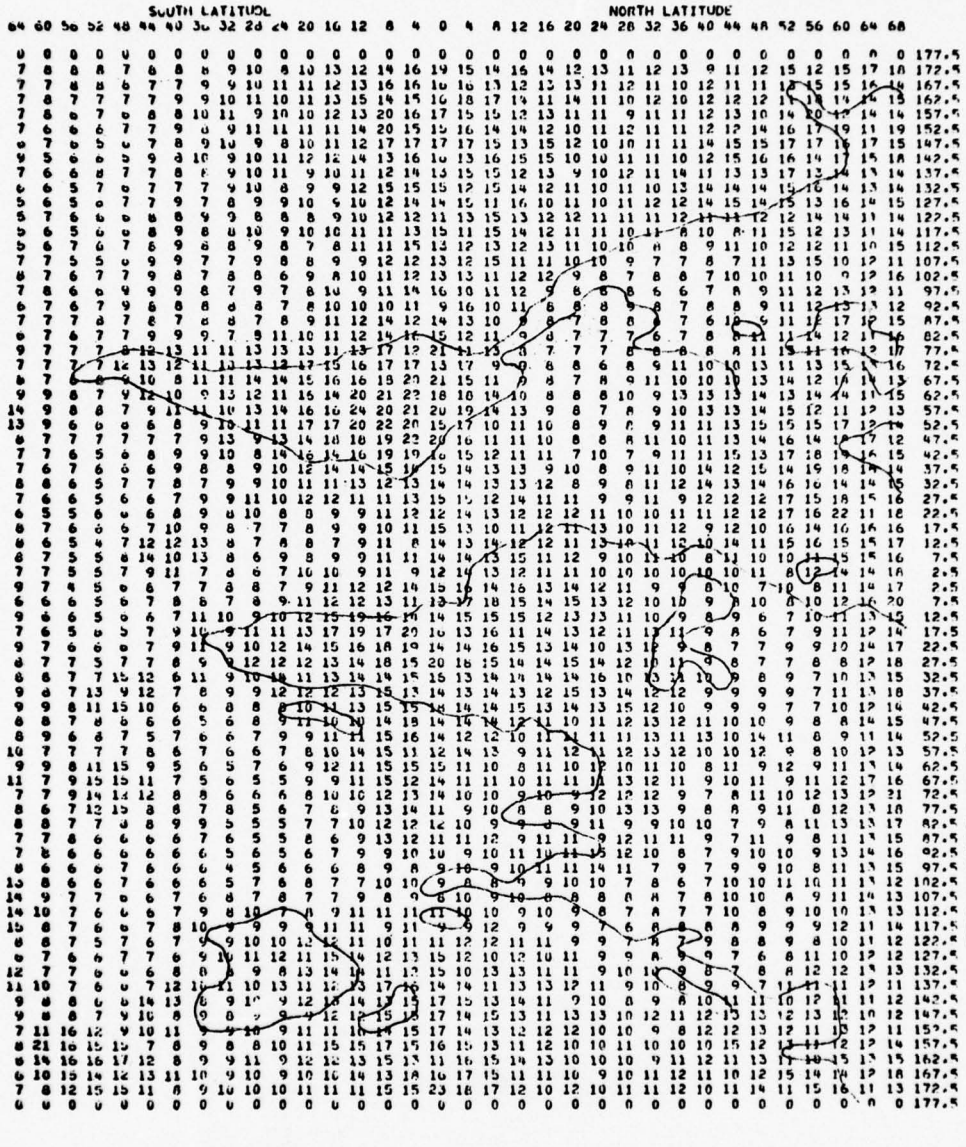

Figure 34 Standard deviation of time-averaged divergence at 500 mb ($x10^{-6}sec^{-1}$).

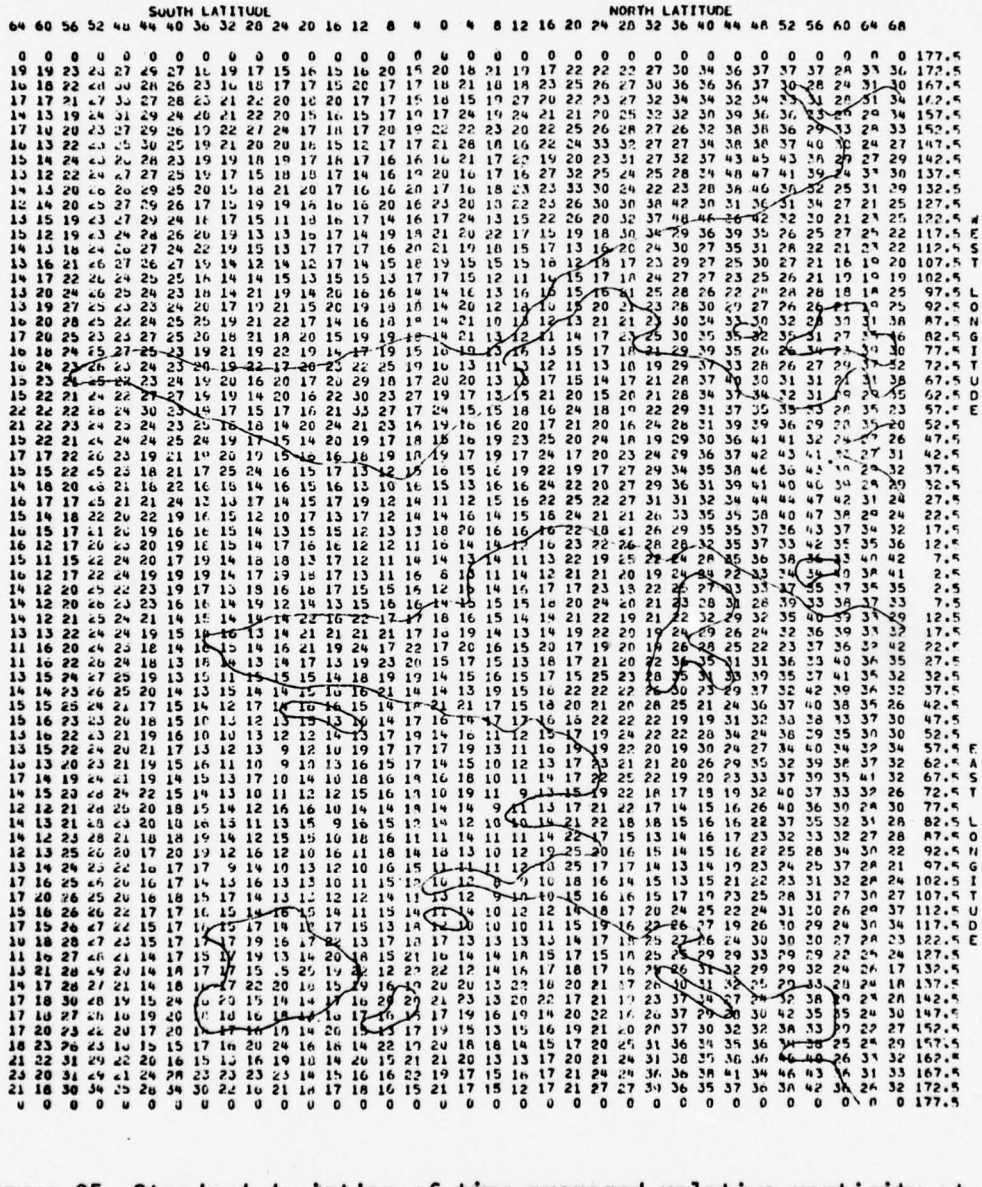

Figure 35 Standard deviation of time-averaged relative vorticity at 500 mb ($x10^{-6}sec^{-1}$).

relatively large positive and negative divergence values.

Although the time-averaged divergence fields do not show patterns which are as organized as the patterns on the time-averaged vorticity charts, there are several clusters of interest. These clusters are best seen at 200 mb where organized areas of positive devergence are present in the tropics over South America, Africa and in the vicinity of Australia. These areas are similar, except for an eastward shift of about 30° longitude, to those which may be inferred from Fig. 1 of Krishnamurti et al, (1973). A smaller cluster is found over and south of India. Also, there is some evidence of organized patterns associated with the Northern Hemisphere jet streams in the Pacific and Atlantic Oceans.

In the Southern Hemisphere tropics, it is interesting to note that the largest standard deviations of the time-averaged divergences generally occur in conjunction with the clusters mentioned above. GOES movie loops show that these regions in South America and Africa often experience extensive diurnal convective development. Thus, one may speculate that the large standard deviations in these areas reflect diurnal oscillations associated with the growth and decay of large scale convection.

Distinct, organized patterns appear in the time-averaged relative vorticity charts in both hemispheres. These patterns correlate well with the jet stream positions which produces confidence in the credibility of the time-averaged vorticity fields. The standard deviations of these fields are of the same order of magnitude as the fields themselves. These patterns imply that the vorticity fields do not vary with time as much as the divergence fields.

CHAPTER IV

KINETIC ENERGY OF THE STANDING WAVES

The distribution of the kinetic energy of the standing eddies and the transient eddies, as a function of wave number was computed. This was done for wave numbers 0 to 36 at both 200 mb and 500 mb by using a Fourier analysis to decompose the time-and-longitudinally averaged kinetic energy into an energy spectrum. Contributions to the kinetic energy from the zonal and meridional wind components were calculated separately.

The energy spectrum for the transient energy is presented in Chapter V, while the spectrum for the standing eddies is covered in this chapter. A comparison of the two energy spectrums is included in the discussion of the results in Chapter V. It should be noted that throughout this discussion the term kinetic energy implies kinetic energy per unit mass, since the total kinetic energy has been defined as

$$KE = \frac{u^2 + v^2}{2} . \tag{4.1}$$

Equation (3.6) defined the time-averaged kinetic energy of the standing eddies (SKE) for each grid point in terms of $\bar{u}$ and $\bar{v}$. However, $\bar{u}$ and $\bar{v}$ are defined by:

$$\bar{u} = u_0 + u' \tag{4.2}$$

and $$\bar{v} = v_o + v' \qquad (4.3)$$

where u_o, v_o are the time-and-longitudinally averaged quantities defined by Equation (3.5) and u', v' represent deviations from the average values. Subsitution for $\bar{u}$ and $\bar{v}$ in Equation (3.5) yields

$$SKE = \frac{(u_o + u')^2}{2} + \frac{(v_o + v')^2}{2} . \qquad (4.4)$$

To find the longitude-averaged standing kinetic energy for a given latitude, Equation (4.4) needs to be integrated around the latitude circle. Since u_o is independent of longitude and u' averaged around a latitude circle is zero, the following result is obtained for the u-component:

$$\frac{1}{2\pi} \int_o^{2\pi} \left(\frac{\bar{u}^2}{2} \right) d\lambda = \frac{u_o^2}{2} + \frac{1}{2\pi} \int_o^{2\pi} \left(\frac{u'^2}{2} \right) d\lambda \qquad (4.5)$$

where $\frac{u_o^2}{2}$ represents the kinetic energy of the stationary zonal motion, wave number zero, and the integral on the right hand side gives the total longitude-averaged kinetic energy of the standing eddies.

It is possible to express $\bar{u}(\lambda r)$ in terms of a Fourier Series as follows:

$$u(\lambda r) = \bar{A}_o + \sum_{m=1}^{n} \left(\bar{A}_m \cos \frac{2\pi\lambda r}{N\Delta\lambda} + \bar{B}_m \sin \frac{2\pi\lambda r}{N\Delta\lambda} \right) \qquad (4.6)$$

where $\Delta\lambda' = a \cos \phi \, \Delta\lambda$,

$\lambda_r = r\Delta\lambda'$

a = radius of the earth,

ϕ = latitude,

N = number of points around latitude circle (72 for this analysis),

$n = N/2$,

and r = index denoting the point on the latitude circle.

The coefficients $\bar{A}_m$ and $\bar{B}_m$, for $m \neq o$, are defined as:

$$\bar{A}_m = \frac{2}{N} \sum_{r=-n}^{n-1} \bar{u}_r \cos \frac{2\pi mr}{N} \tag{4.7}$$

and

$$\bar{B}_m = \frac{2}{N} \sum_{r=-n}^{n-1} \bar{u}_r \sin \frac{2\pi mr}{N} \, , \tag{4.8}$$

Since n is even, $\bar{B}_n$ is zero. For m = o,

$$\bar{A}_o = \frac{1}{N} \sum_{r=-n}^{n-1} \bar{u}_r \quad \text{and} \quad B_o = o.$$

Using the Fourier Series expansion for u and Parseval's Theorem, it is possible to express the longitude-averaged standing kinetic engergy as:

$$\frac{1}{2\pi} \int_o^{2\pi} \left(\frac{\bar{u}^2}{2}\right) d\lambda = \frac{1}{2N} \sum_{r=-n}^{n-1} \bar{u}_r^2 = \frac{\bar{A}_o^2}{2} + \frac{1}{4} \sum_{m=1}^{n} (\bar{A}_m^2 + \bar{B}_m^2). \tag{4.9}$$

Comparing Equation (4.5) and (4.9) leads to the conclusion that

$$\overline{A}_o^2 = u_o^2 \tag{4.10}$$

and

$$\frac{1}{2\pi} \int_0^{2\pi} (u')^2 d\lambda = \frac{1}{2} \sum_{m=1}^{n} (\overline{A}_m^2 + \overline{B}_m^2) . \tag{4.11}$$

From Equation (4.11) it is evident that the contribution to the longitude-averaged kinetic energy of the standing eddies for a given wave number (SKE_m) can be computed as follows:

$$SKE_m = \frac{\overline{A}_m^2 + \overline{B}_m^2}{2} . \tag{4.12}$$

Longitudinal averages of kinetic energy for the meridional wind components are found in the same manner by replacing u quantities by the corresponding v quantities.

Equation (4.12) was used to calculate the values of SKE_m for wave numbers 0 to 36 at fourteen latitudes. Values for u and v components were computed separately. The results for wave numbers 0 to 18 are contained in Table 3.

Analysis of these results did not produce anything unexpected. In mid-latitudes much of the standing kinetic energy is contained in wave number zero of the u component. At 200 mb for the u component, there is a shift of the energy to wave numbers 2, 3, and 4 near the equator. In fact, at 4° S and 4° N wave number zero contains essentially no energy at 200 mb. However, at 500 mb the maximum energy is still contained in wave number zero. The increase in the total 200 mb standing

TABLE 3

Decomposed Standing Kinetic Energy for Wave Numbers 0-18

KE FOR U COMPONENT AT 200 MB

LAT																			TOTAL
52	206	12	15	4	0	0	0	0	0	0	0	0	0	0	0	0	0	0	238
44	346	19	25	7	1	0	1	0	0	0	0	0	0	0	0	0	0	0	400
36	497	34	17	22	0	1	0	0	0	0	0	0	0	0	0	0	0	0	574
28	721	98	1	34	3	0	2	0	0	0	0	0	0	0	0	0	0	0	860
20	349	19	3	2	0	0	2	1	0	0	0	0	0	0	0	0	0	0	377
12	45	25	3	7	1	1	0	0	0	0	0	0	0	0	0	0	0	0	83
4	1	36	28	10	4	1	1	0	0	0	0	0	0	0	0	0	0	0	85
-4	0	32	43	20	8	2	1	1	0	0	0	0	0	0	0	0	0	0	110
-12	4	5	14	10	7	1	2	1	0	1	1	0	0	0	0	0	0	0	49
-20	2	1	1	0	4	2	1	1	0	0	0	0	0	0	0	0	0	0	15
-28	91	0	12	6	8	1	1	0	0	0	0	0	0	0	0	0	0	0	122
-36	213	1	0	1	1	0	0	0	0	0	0	0	0	0	0	0	0	0	217
-44	404	5	2	2	0	0	1	0	0	0	0	0	0	0	0	0	0	0	415
-52	313	15	0	0	3	1	1	0	0	0	0	0	0	0	0	0	0	0	332

K	0	1	2	3	4	5	6	7	8	9	10	11	12	13	14	15	16	17	18

KE FOR V COMPONENT AT 200 MB

LAT																			TOTAL
52	0	1	10	12	2	1	1	0	0	0	0	0	0	0	0	0	0	0	27
44	0	1	1	8	0	1	1	1	0	0	0	0	0	0	0	0	0	0	14
36	0	1	0	2	0	1	2	1	1	0	0	0	0	0	0	0	0	0	9
28	0	1	2	7	0	1	1	0	1	0	0	0	0	0	0	0	0	0	14
20	1	5	3	12	1	0	1	0	0	0	0	0	0	0	0	0	0	0	24
12	1	2	3	5	0	1	1	1	0	0	0	0	0	0	0	0	0	0	18
4	1	2	4	1	0	0	0	1	0	0	0	0	0	0	0	0	0	0	12
-4	0	0	1	0	2	2	0	0	1	0	0	0	0	0	0	0	0	0	8
-12	0	1	2	4	4	0	0	0	1	1	1	0	0	0	0	0	0	0	17
-20	0	2	3	4	4	0	1	0	0	1	0	0	0	0	1	1	0	0	27
-28	0	0	0	1	5	1	3	2	1	1	0	0	0	0	0	0	0	0	22
-36	0	0	0	0	4	1	5	1	1	0	0	0	0	0	0	0	0	0	13
-44	0	0	0	0	4	2	3	0	0	0	0	0	0	0	0	0	0	0	10
-52	0	0	0	1	3	1	1	0	0	0	0	0	0	0	0	0	0	0	7

K	0	1	2	3	4	5	6	7	8	9	10	11	12	13	14	15	16	17	18

KE FOR U COMPONENT AT 500 MB

LAT																			TOTAL
52	76	6	7	4	0	1	0	0	0	0	0	0	0	0	0	0	0	0	95
44	148	14	12	6	1	0	1	0	0	0	0	0	0	0	0	0	0	0	182
36	122	5	3	7	0	1	0	0	0	0	0	0	0	0	0	0	0	0	139
28	107	18	1	11	0	0	0	0	0	0	0	0	0	0	0	0	0	0	139
20	67	13	2	4	1	0	1	0	0	0	0	0	0	0	0	0	0	0	88
12	1	2	1	4	0	1	0	0	0	0	0	0	0	0	0	0	0	0	9
4	6	3	0	1	0	0	0	0	0	0	0	0	0	0	0	0	0	0	12
-4	2	1	0	0	1	1	0	0	0	0	0	0	0	0	0	0	0	0	6
-12	3	2	0	1	1	0	0	0	0	0	0	0	0	0	0	0	0	0	9
-20	3	0	0	0	1	0	0	0	0	0	0	0	0	0	0	0	0	0	6
-28	12	0	2	1	2	0	0	0	0	0	0	0	0	0	0	0	0	0	19
-36	70	2	1	3	1	0	0	0	0	0	0	0	0	0	0	0	0	0	77
-44	212	0	2	2	0	0	0	0	0	0	0	0	0	0	0	0	0	0	218
-52	165	5	0	0	1	0	0	0	0	0	0	0	0	0	0	0	0	0	172

K	0	1	2	3	4	5	6	7	8	9	10	11	12	13	14	15	16	17	18

KE FOR V COMPONENT AT 500 MB

LAT																			TOTAL
52	0	1	4	6	1	1	0	0	0	0	0	0	0	0	0	0	0	0	16
44	0	0	1	6	1	1	0	0	0	0	0	1	0	0	0	0	0	0	10
36	0	1	0	3	0	0	1	1	0	0	0	0	0	0	0	0	0	0	7
28	0	0	0	0	0	0	0	0	0	0	0	0	0	0	0	0	0	0	4
20	0	0	1	1	0	0	0	0	0	0	0	0	0	0	0	0	0	0	4
12	0	0	0	0	0	0	0	0	0	0	0	0	0	0	0	0	0	0	2
4	0	0	0	0	0	0	0	0	0	0	0	0	0	0	0	0	0	0	1
-4	0	0	0	0	0	0	0	0	0	0	0	0	0	0	0	0	0	0	2
-12	0	0	0	0	0	0	0	0	0	0	0	0	0	0	0	0	0	0	2
-20	0	0	0	0	0	0	0	0	0	0	0	0	0	0	0	0	0	0	3
-28	0	0	0	0	0	0	0	0	0	0	0	0	0	0	0	0	0	0	4
-36	0	0	0	0	1	1	1	0	0	0	0	0	0	0	0	0	0	0	4
-44	0	0	0	0	2	0	1	0	0	0	0	0	0	0	0	0	0	0	4
-52	0	0	0	1	2	0	0	0	0	0	0	0	0	0	0	0	0	0	4

K	0	1	2	3	4	5	6	7	8	9	10	11	12	13	14	15	16	17	18

kinetic energy at 4° S is a reflection of the mid-Pacific jet.

For all latitudes there is little detectable energy above wave number 5. Another contrast between 200 mb and 500 mb is the latitude at which the maximum total KE occurs in the Northern Hemisphere. At 200 mb the maximum occurs at 28° N latitude, while the 500 mb maximum occurs at 44° N. The same trend appears in the distribution of maximum energy for wave number zero. This indicates that the maximum kinetic energy at 200 mb is associated with the sub-tropical jet, while the maximum energy at 500 mb occurs in conjunction with the polar jet. It is obvious from this example that an apparent trend at one level of the atmosphere cannot always be extrapolated to a different level.

The v component shows a preference for wave number three in the Northern Hemisphere and wave number four in the Southern Hemisphere at both 200 mb and 500 mb. The 200 mb total column shows a maximum in the sub-tropics in both hemispheres, but the 500 mb v component has only one significant maximum at 52° N. This again suggests that the maximum energy at 500 mb is associated with the polar front. At 200 mb it appears there is about as much standing kinetic energy of the v component associated with the polar jet as with the sub-tropical jet. The results obtained from the spectral analysis of the DST data agree with the general features of those reported in other investigations (see i.e., Kao and Wendell, 1970).

Also, Winn-Nielson (1967) found that the N.H. maximum of the zonal kinetic energy occurred in February and the minimum occurred in July. Thus, it can be assumed that the values given in Table 3 represents approximate maximum values for the Northern Hemisphere and minimum values for the Southern Hemisphere.

CHAPTER V

KINETIC ENERGY OF TRANSIENT WAVES

The time-and-longitude averaged kinetic energy for the transient waves was decomposed in wave number space in a manner similiar to that described in Chapter IV. The transient part of the flow is defined as the instantaneous departure from the time-averaged flow as follows:

$$u^* = u - \bar{u} \tag{5.1}$$

and

$$v^* = v - \bar{v} \tag{5.2}$$

where $\bar{u}$, $\bar{v}$ are defined by equations (3.1) and (3.2),

u, v are the actual wind components for each observation

and u^*, v^* are the components of the transient flow.

Substitution of u_r^* for $\bar{u}_r$ in Equation (4.9), results in the following equation for the longitude-averaged transient energy:

$$\frac{1}{2\pi}\int_0^{2\pi}\frac{(u^*)^2}{2}d\lambda = \frac{1}{2N}\sum_{r=-n}^{n-1}(u_r^*)^2 = \frac{A_0^{*2}}{2} + \frac{1}{2}\sum_{m=1}^{n}(A_m^{*2} + B_m^{*2}) \tag{5.3}$$

where A_m^* and B_m^*, for $m \neq o$, are defined by

$$A_m^* = \frac{2}{N}\sum_{r=-n}^{n-1} u_r^* \cos\frac{2\pi mr}{N} \tag{5.4}$$

and

$$B_m^* = \frac{2}{N} \sum_{r=-n}^{n-1} u_r^* \sin \frac{2\pi mr}{N} \quad . \tag{5.5}$$

For $m = o$, $A_o^* = \frac{1}{N} \sum_{r=-n}^{n-1} u_r^*$ and $B_o^* = o$.

All quantities except the starred ones are defined the same as in Chapter IV. To calculate the time-and-longitude averaged transient energy, it is necessary to integrate Equation (5.3) over the time period in the following manner:

$$\frac{1}{2\pi T} \int_o^T \int_o^{2\pi} \frac{(u^*)^2}{2} d\lambda dt = \frac{1}{2NT} \int_o^T \left(\sum_{r=-n}^{n-1} \cdot u_r^{*2} \right) dt$$

$$= \frac{1}{T} \int_o^T \left(\frac{A_o^{*2}}{2} + \frac{1}{4} \sum_{m=1}^{n} (A_m^{*2} + B_n^{*2}) \right) dt \quad . \tag{5.6}$$

Moving the integral on the right hand side of Equation (5.6) inside the wave number summation and replacing it with a summation over time yields:

$$\frac{1}{T} \int_o^T \frac{1}{2N} \left(\sum_{r=-n}^{n-1} u_r^{*2} \right) dt = \frac{1}{M} \sum_{i=1}^{M} \frac{A_o^{*2}}{2} + \frac{1}{4M} \sum_{m=1}^{n} \left[\sum_{i=1}^{M} (A_m^{*2} + B_m^{*2})_i \right] \tag{5.7}$$

where $M = 70$.

If it is considered that the transient flow is composed of a

zonally average value and a deviation from this average, u* can be written as

$$u^* = u_o^* + u^{*'}$$

where u_o^* = transient part of zonal average

and $u^{*'}$ = transient eddy.

Applying the above definition to the terms on the right hand side of Equation (5.7) results in $A_o^{*2} = u_o^{*2}$ and

$$\frac{1}{2\pi T}\int_o^T\int_o^{2\pi}\frac{(u^{*'})^2}{2}d\lambda dt = \frac{1}{4M}\sum_{m=1}^{n}\left[\sum_{i=1}^{M}(A_m^{*2} + B_m^{*2})_i\right].$$

Thus, the contribution to the time-and-longitude average transient kinetic energy for each wave number ($\widetilde{TKE}_m$) can be computed from

$$\widetilde{TKE}_m = \frac{1}{4M}\sum_{i=1}^{M}(A_m^{*2} + B_m^{*2})_i \quad . \tag{5.8}$$

The results of using Equation (5.8) to compute the values of $\widetilde{TKE}_m$ are presented in Table 4. The latitudes and wave numbers are the same as for the standing eddies.

Again the results are not unexpected. Table 4 shows several contrasts when compared with Table 3. The total transient kinetic energy of the u component is much smaller than the standing kinetic energy in mid-latitudes. At the equator, the contributions from the u components are about the same magnitude for the transient and standing kinetic energies. For the v components the transient kinetic energy is significantly larger than the standing kinetic energy at all latitudes.

TABLE 4

Decomposed Time-averaged Transient Kinetic Energy for Wave Numbers 0-18

KE FOR U COMPONENT AT 200 MB

LAT																			TOTAL
52	8	18	11	17	9	8	7	4	3	2	1	1	1	1	0	0	0	0	94
44	6	22	14	20	11	10	4	6	4	2	1	1	1	1	1	1	1	0	111
36	4	8	24	19	10	9	7	6	7	3	2	1	1	1	1	1	1	1	110
28	3	17	17	19	13	10	7	6	4	3	2	2	2	2	1	1	1	1	117
20	6	10	9	5	6	6	4	4	2	2	2	1	1	1	1	1	1	1	71
12	3	9	9	6	3	6	4	2	3	2	1	2	1	2	1	2	1	1	67
4	4	6	6	8	5	3	3	2	3	2	1	2	2	2	2	1	1	1	69
-4	4	6	5	6	5	5	3	4	3	3	2	2	2	2	1	2	2	1	75
-12	2	6	4	6	4	6	4	3	3	2	2	3	2	1	1	1	1	2	66
-20	2	4	6	6	8	4	3	4	2	2	2	1	2	2	2	1	1	1	63
-28	3	5	9	6	5	7	4	5	5	3	2	2	1	1	2	1	1	1	69
-36	3	4	12	13	8	10	5	4	3	4	3	2	2	2	1	1	1	1	84
-44	1	11	7	6	7	4	3	3	2	2	2	1	2	1	1	1	0	1	60
-52	2	9	9	5	5	7	3	4	2	1	2	2	1	1	1	1	1	0	56

K	0	1	2	3	4	5	6	7	8	9	10	11	12	13	14	15	16	17	18

KE FOR V COMPONENT AT 200 MB

LAT																			TOTAL
52	0	2	8	12	21	16	10	11	6	4	2	2	1	1	1	1	1	0	105
44	0	1	4	10	14	16	13	15	12	6	3	3	2	2	1	1	1	1	113
36	0	2	2	5	9	19	12	16	15	8	4	4	3	2	1	1	1	1	112
28	0	1	4	4	5	16	9	15	13	8	3	3	3	2	2	1	1	1	105
20	1	1	4	5	4	8	6	8	8	6	3	3	3	2	1	1	1	1	81
12	1	2	3	2	3	4	3	4	4	4	2	2	2	1	1	1	1	1	61
4	1	2	3	3	3	4	3	4	3	2	2	2	1	1	1	1	1	1	58
-4	1	1	2	3	2	4	2	2	3	2	2	2	1	1	1	1	1	1	54
-12	1	1	1	1	1	2	2	3	2	2	3	1	2	2	1	1	1	2	1	54
-20	0	1	1	1	2	3	3	4	3	3	4	2	2	2	1	2	2	2	2	65
-28	1	1	1	2	3	5	6	4	5	5	5	4	2	3	2	2	1	1	1	73
-36	1	1	2	2	4	9	7	7	5	5	4	3	2	2	1	1	1	1	1	71
-44	0	1	2	4	6	14	7	12	5	4	4	3	2	2	2	1	1	1	1	85
-52	0	1	2	5	6	9	6	7	5	4	4	3	2	2	1	1	1	1	1	68

K	0	1	2	3	4	5	6	7	8	9	10	11	12	13	14	15	16	17	18

KE FOR U COMPONENT AT 500 MB

LAT																			TOTAL
52	7	14	11	15	8	7	4	3	3	1	1	1	1	1	1	0	0	0	82
44	3	15	9	14	6	6	3	3	3	2	2	1	1	1	1	0	0	0	77
36	4	6	8	6	6	4	3	3	3	2	2	1	1	1	1	1	0	0	57
28	3	7	8	9	6	4	4	3	2	1	1	1	1	1	1	1	0	0	58
20	2	3	5	4	4	3	2	2	2	1	1	1	1	1	0	0	1	0	39
12	2	2	3	3	2	2	1	1	2	1	1	1	1	0	1	1	1	1	33
4	2	3	3	3	2	2	2	1	1	1	1	1	1	1	1	1	1	1	36
-4	1	2	1	2	2	1	1	1	1	1	1	1	1	1	1	1	1	1	33
-12	1	3	3	2	2	1	1	1	1	1	1	1	1	1	1	1	1	1	35
-20	1	2	3	2	3	1	1	1	1	1	1	1	1	1	1	1	1	0	27
-28	1	2	3	2	2	2	1	1	1	1	1	1	0	1	1	0	0	0	0	24
-36	1	4	3	4	3	4	2	2	1	1	1	1	1	1	1	0	0	0	0	30
-44	2	6	3	5	4	2	2	2	2	1	1	1	1	0	0	0	0	0	0	33
-52	1	6	4	2	4	4	1	2	1	1	1	1	0	0	0	0	0	0	0	31

K	0	1	2	3	4	5	6	7	8	9	10	11	12	13	14	15	16	17	18

KE FOR V COMPONENT AT 500 MB

LAT																			TOTAL
52	0	1	4	7	15	13	8	10	5	4	2	3	2	1	1	2	1	1	87
44	0	1	3	6	10	9	8	12	9	4	4	2	2	2	2	2	1	1	84
36	0	1	1	4	5	9	7	9	8	4	3	3	2	2	1	1	1	1	69
28	0	1	1	2	2	5	3	5	5	3	2	2	1	1	1	1	1	1	43
20	0	1	1	1	2	2	2	3	3	2	1	2	1	1	1	1	0	1	32
12	0	1	1	1	1	1	1	2	2	1	1	1	1	1	0	1	1	1	27
4	1	1	1	1	1	1	1	1	1	1	1	1	1	1	1	1	1	1	33
-4	1	1	1	1	1	2	1	1	1	1	1	1	1	1	1	1	1	1	31
-12	0	1	1	1	1	1	1	1	1	1	1	1	1	1	1	1	1	1	26
-20	0	0	0	1	1	1	1	1	1	1	1	1	1	1	1	1	1	1	21
-28	0	0	0	1	1	1	2	1	1	1	1	1	1	1	1	0	0	0	21
-36	0	0	1	1	2	3	2	2	2	1	2	1	1	1	1	0	0	0	27
-44	0	0	1	2	3	6	3	4	3	2	2	2	1	1	1	1	0	0	37
-52	0	0	1	3	3	4	3	4	3	3	3	2	1	1	1	1	1	1	40

K	0	1	2	3	4	5	6	7	8	9	10	11	12	13	14	15	16	17	18

Also, the distribution of energy with respect to wave number is different for the transient energy.

The transient kinetic energy of the u component is concentrated in wave numbers 1 to 4 with only a small amount of the total in wave number one. For the v component the transient kinetic energy is clustered between wave numbers 3 and 8. However, in the tropics, the transient energy is spread out fairly evenly over all the wave numbers. This implies that there is no dominate mechanism in the tropics in this data set which can be associated with the transient kinetic energy.

It should also be noted that some of the kinetic energy in the larger wave numbers may be due to gravity type waves. Some are probably real but others may be induced by the numerical approximations of the model.

The supposition that the model is producing some spurious waves results from the fact that at some latitudes there was an increase in the kinetic energy around wave numbers 33-36.

CHAPTER VI

SUMMARY AND CONCLUSIONS

The analyses presented here indicate that the DST data assimilated by the GISS model is useful for global studies of the general atmospheric circulation. The time-averaged charts presented in Chapter III correlated very well with previously produced charts. A close look at the time-averaged charts reveals that this data set is only valid between about 60° S and 60° N. Poleward of these latitudes there are many places where two or more grid points have the same values. Lack of sufficient data and the closeness of grid points probably contributed to this duplication. Given sufficient data to totally initialize the grid, the GISS model should provide fine quality data for the entire globe. A positive feature of the DST data is the ease with which it can be handled in horizontal arrays.

Interpolation of the wind components from sigma levels to constant pressure levels by a cubic spline appears to have been very successful. There was some concern as to the effectiveness of interpolating the π fields to wind data points, however, the results support the technique used here.

The success of this technique suggests it could be used to generate winds at most any level, between the top and bottom sigma levels, for which winds are desired. By making full use of the vertical resolution of the model, it should be possible to see the time-and-longitude

averaged meridional circulation in more detail.

It was encouraging to see significate, though small, values of the time-and-longitude averaged meridional wind component which were organized into patterns. Also, the time-averaged values of the meridional wind show organized wave patterns in both hemispheres which are very well defined. Thus, the winds in this data set are much less constrained than in earlier studies.

An original objective of this research was to study the DST divergence fields. The time-averaged divergence showed areas of organization, especially at 200 mb, indicating that the DST data can be used for divergence studies. However, it is uncertain how much detail can be resolved in the divergence fields. The randomness observed in some areas of Figures 26 to 31 may be due to some partial contamination by gravity type waves. This conclusion results from the fact that an increase was observed in the kinetic energy for high wave numbers at some latitudes. Another source of uncertainty for both the vorticity and divergence fields is the mountain effect on the fields. This effect was discussed in Chapter II and was probably greatly reduced by the interpolation to constant pressure levels.

Wave number decomposition of the kinetic energy spectrum around latitude circles is easy to accomplish because of the structure of the grid. Although there were no surprises in the results from Chapter IV and Chapter V, it was noted that there is some difference between the relative amounts of energy carried by waves of a certain wave number at different levels. Thus, to adequately describe the energy transport in the atmosphere, it is important to consider several vertical levels.

Most of the features observed in the data conformed to previously calculated averages. The 200 mb mid-Pacific trough over the equator stands out as a subject worthy of future research. From this data it appears that flow from south of the equator is feeding into the sub-tropical jet which extends across Central America. A study of the energy transfer involved in this process could prove to be very interesting and informative.

REFERENCES

Conte, S.D., and Carl de Boor, 1972: Elementary Numerical Analysis: An Algorithmic Approach, McGraw-Hill Book Company, New York, 233-240.

Heastie, H., and P.M. Stephenson, 1960: Upper winds over the world. Parts I and II. Geophys. Mem. No. 103, Meteor. Off. London, H.M. Stationery Off., 217 pp.

Kao, S.K., and L.L. Wendell, 1970: The kinetic energy of the large-scale atmospheric motion in wavenumber-frequency space, Journal of the Atmospheric Sciences, 27, 359-375.

Krishnamurti, T.N., M. Kanamitsu, W.J. Koss, and J.D. Lee, 1973: Tropical east-west circulations during the northern winter, Journal of the Atmospheric Sciences, 30, 780-787.

Lorenz, E.N., 1967: The Nature and Theory of the General Circulation of the Atmosphere, World Meteorological Organization.

Namias, J., 1963: Interactions of circulation and weather between hemispheres, Monthly Weather Review, 91, 482-486.

Oort, A.H., and E.M. Rasmusson, 1971: Atmospheric circulation statistics, NOAA Professional Paper 5, Rockville, Md.

Phillips, N.A., 1957: A coordinate system having some special advantages for numerical forecasting, Journal of Meteorology, 14, 184-185.

Sadler, J.C., 1975: The upper tropospheric circulation over the global tropics, UHMET-75-05, Dept. of Meteorology, University of Hawaii.

Somerville, R.C.J., P.H. Stone, M. Halem, J.E. Hansen, J.S. Hogan, L.M. Druyan, G. Russel, A.A. Lacis, W.J. Quirk, and J. Tenenbaum, 1974: The GISS model of the global atmosphere, Journal of the Atmospheric Sciences, 31, 84-117.

Van Loon, H., J.J. Taljaard, R.L. Jenne, and H.L. Crutcher, 1971: Climate of the upper air: southern hemisphere. Vol. II, Zonal Geostrophic Winds. NCAR TN/STR-57 and NAVAIR 50-1C-56, Boulder, Colo., National Center for Atmospheric Research, 43 pp.

Winn-Nielson, A., 1967: On the annual variation and spectral distribution of atmospheric energy, Tellus, XIX (4), 540-559.

VITA

Name	Allan Joseph McGlasson
Birthplace	Corvallis, Oregon
Birthdate	April 13, 1945
High School	LaGrande Senior High School LaGrande, Oregon
University 1963-1967	Oregon State University Corvallis, Oregon
College 1967-1969	Eastern Oregon State College LaGrande, Oregon
University 1969-1970 1976-1977	University of Utah Salt Lake City, Utah
Degrees 1967	B.S., Oregon State University Corvallis, Oregon
1970	B.S., University of Utah Salt Lake City, Utah
Honorary Societies	Phi Kappa Phi, Chi Epsilon Pi
Professional Position	Weather Officer United States Air Force